The Astrophysical Journal, 931:38 (24pp), 2022 May 20 https://doi.org/10.3847/1538-4357/ac666f
© 2022. The Author(s). Published by the American Astronomical Society.
OPEN ACCESS

Linking Characteristics of the Polycyclic Aromatic Hydrocarbon Population with Galaxy Properties: A Quantitative Approach Using the NASA Ames PAH IR Spectroscopic Database

A. Maragkoudakis[1,2], C. Boersma[1], P. Temi[1], J. D. Bregman[1], and L. J. Allamandola[1]
[1] NASA Ames Research Center, MS 245-6, Moffett Field, CA 94035-1000, USA; maragkoudakis.alex@gmail.com
[2] Oak Ridge Associated Universities, Oak Ridge, TN, USA
Received 2022 February 18; revised 2022 March 31; accepted 2022 April 10; published 2022 May 23

Abstract

Utilizing the data and tools provided through the NASA Ames PAH IR Spectroscopic Database (PAHdb), we study the PAH component of over 900 Spitzer-IRS galaxy spectra. Employing a database-fitting approach, the average PAH size, the PAH size distribution, and PAH ionization fraction are deduced. In turn, we examine their connection with the properties of the host galaxy. We found that PAH population within galaxies consists of middle-sized PAHs with an average number of carbon atoms of $\overline{N_C} = 55$, and a charge state distribution of ∼40% ionized—60% neutral. We describe a correlation between the 6.2/11.2 μm PAH ratio with the ionization parameter ($\gamma \equiv (G_0/n_e)(T_{gas}/1\ \mathrm{K})^{0.5}$), a moderate correlation between the 8.6/11.2 μm PAH ratio and specific star formation rate, and a weak anticorrelation between γ and M_*. From the PAHdb decomposition, we provide estimates for the 3.3 μm PAH band, not covered by Spitzer observations, and establish a correlation between the 3.3/11.2 μm PAH ratio with N_C. We further deliver a library of mid-IR PAH template spectra parameterized on PAH size and ionization fraction, which can be used in galaxy spectral energy distribution fitting codes for the modeling of the mid-IR PAH emission component in galaxies.

Unified Astronomy Thesaurus concepts: Interstellar molecules (849); Interstellar line emission (844); Infrared sources (793); Interstellar medium (847)

1. Introduction

The mid-infrared (mid-IR) spectra of numerous astrophysical sources, such as planetary and reflection nebula, the interstellar medium (ISM), and star-forming regions, and consequently of entire galaxies, are dominated by prominent emission features at 3.3, 6.2, 7.7, 8.6, 11.2, and 12.7 μm, attributed to polycyclic aromatic hydrocarbons (PAHs; Leger & Puget 1984; Allamandola et al. 1985). Extensive observations from the Infrared Space Observatory (ISO) and the Spitzer Space Telescope have established the omnipresence of PAH emission in galaxies in both the local and high-redshift universe (e.g., Genzel et al. 1998; Rigopoulou et al. 1999; Armus et al. 2007; Gordon et al. 2008; O'Dowd et al. 2009; Riechers et al. 2014; Li 2020), as well as in diverse galactic environments, i.e., dominated by either star formation, active galactic nuclei (AGN) activity, or a combination thereof (e.g., Smith et al. 2007; Alonso-Herrero et al. 2014; Esparza-Arredondo et al. 2018).

Emission from PAHs has been extensively used as a tool in galactic and extragalactic studies, as the spectral characteristics can be directly tied to the prevailing local astrophysical conditions of the emitting regions. This is because the spectrum is a reflection of the composition of the underlying PAH population, which, in turn, is determined by the astrophysical and astrochemical environment. For example, their abundance and emission properties depend on the metallicity and radiation field characteristics (e.g., Galliano et al. 2008; Sandstrom et al. 2012). However, PAHs do not only passively respond to their environment, but also drive many of its aspects, e.g., they regulate the charge balance through their high electron affinity (e.g., Bakes & Tielens 1994). Via a set of empirical relations, PAH emission is employed to infer the local physical conditions (i.e., the strength of the local UV field, G_0, electron density, n_e, and gas temperature, T_{gas}), in both resolved galactic sources (e.g., Fleming et al. 2010; Rosenberg et al. 2011; Boersma et al. 2015) and galaxies (e.g., Galliano et al. 2008). Furthermore, for galaxies in particular, PAH luminosity has been calibrated and used as a tracer of the integrated and spatially resolved star formation rate (SFR), particularly for metal-rich and dust-rich galactic environments (e.g., Calzetti et al. 2007; Shipley et al. 2016; Maragkoudakis et al. 2018b).

PAH emission can be responsible for some 5%–30% of the total IR emission observed from galaxies (Helou et al. 2000; Smith et al. 2007), which establishes their significance. In galaxy studies, the modeling of the spectral energy distribution (SED) from (spectro-)photometric observations has grown in popularity over the recent years as a method for determining global and spatially resolved galaxy properties (Conroy 2013; Ciesla et al. 2014; Chevallard & Charlot 2016; Ciesla et al. 2018; Nersesian et al. 2019; Enia et al. 2020; Johnson et al. 2021). Its applicability relies heavily on a proper modeling of the entire mid-IR spectrum, as getting the energy balance correct plays a crucial role. That is, the energy absorbed by dust and PAHs in the UV-optical range directly translates to the energy emitted in the mid- and far-IR domain. Therefore, a robust framework and modeling of the three main "dust" components: PAHs; very small warm grains (VSGs); and large relatively cold grains (responsible for the emission beyond $\lambda \sim 100\ \mu$m), are essential in galaxy studies.

The implementation of the PAH emission component in dust emission models (e.g., Draine & Li 2007; Draine et al. 2014; Dale et al. 2014) is considered not yet complete. The dust

Original content from this work may be used under the terms of the Creative Commons Attribution 4.0 licence. Any further distribution of this work must maintain attribution to the author(s) and the title of the work, journal citation and DOI.

Table 1
Summary of Galaxy Sample Properties per Legacy Program

Program	N_{gal}[a]	z	SFR $[M_\odot\ yr^{-1}]$	M_* $[M_\odot]$	Z[b]
SINGS	57	$0.0006 \leqslant z \leqslant 0.02$	$-1.5 < \log(SFR) < 1.0$	…	$7.81 < Z < 8.6$
SSGSS	94	$0.03 \leqslant z \leqslant 0.2$	$-0.9 \leqslant \log(SFR) \leqslant 1.8$	$9.2 \leqslant \log(M_*) \leqslant 11.3$	$8.5 \leqslant Z \leqslant 8.9$
S5	291	$0.05 < z < 0.1$	$-1.2 \leqslant \log(SFR) \leqslant 1.6$	$9.1 \leqslant \log(M_*) \leqslant 11.5$	$8.2 \leqslant Z \leqslant 8.8$
GOALS	189	$0.003 < z < 0.09$	$1.2 \leqslant \log(SFR) \leqslant 2.7$	$10.3 \leqslant \log(M_*) \leqslant 11.8$	…
5MUSES	279	$0.02 < z < 0.2$	$-0.9 \leqslant \log(SFR) \leqslant 1.8$	$9.4 \leqslant \log(M_*) \leqslant 11.4$	$8.4 \leqslant Z \leqslant 8.8$

Notes.
[a] Total number of galaxies from each program considered here.
[b] $12 + \log(O/H)$.

emission models of Draine & Li (2007), for instance, are based on a dust mixture of amorphous silicate and graphite grains, as well as PAHs. These models separate dust emission into: (i) diffuse emission from the general stellar dust population, and (ii) emission from dust that is connected to star-forming regions, illuminated with a variable radiation field and parameterized with the fraction of PAHs locked up in the total dust mass (q_{PAH}). These approaches typically do not take into account the effect of PAH structure and/or symmetry on the emerging spectrum, which can be significant (e.g., Boersma et al. 2010; Andrews et al. 2015). Furthermore, the high spectral resolution observations to be returned by the James Webb Space Telescope (JWST) are expected to reveal unprecedented insight into the PAH (sub-)populations and (sub-)features, whose emission characteristics are highly sensitive to molecular edge structure (e.g., Peeters et al. 2017).

The goals of this work include supplementing and enhancing the PAH emission component of galaxy dust emission models by delivering a set of galaxy PAH emission spectral templates, derived from a large collection of PAH molecules of various sizes, molecular edge structures, and in different charge states. To achieve this, we performed a quantitative examination of the PAH characteristics in different galactic environments and their connection with fundamental galaxy properties (i.e., SFR, specific SFR (sSFR), stellar mass (M_*), strength of the (local) radiation field (G_0), and metallicity (Z)), utilizing the NASA Ames PAH IR Spectroscopic Database[3] (hereafter PAHdb; see Boersma et al. 2014b; Bauschlicher et al. 2018; Mattioda et al. 2020). PAHdb data, models, and software tools have already been successfully employed to probe the PAH properties in interstellar medium (ISM) sources (Cami et al. 2010; Boersma et al. 2013, 2014b, 2014a, 2015, 2018; Zang et al. 2019; Shannon & Boersma 2019). Furthermore, we aim to establish whether PAH band strength ratios can be empirically calibrated into quantitative PAH ionization fractions (f_i) and/or the PAH ionization parameter γ, with the latter linking PAH ionization with G_0, n_e, and T_{gas}, as has been successfully done for ISM sources. This work relies on the combined data from five Spitzer Legacy Programs, culminating in over 900 spectra (see Section 2). The work described here, referred to as Paper I, will be followed up by another paper (Paper II) that will go into deeper detail regarding the sensitivity of the results to different model components, band strength measuring methods, pools of PAH molecules, and spectral wavelength range.

This paper is structured as follows: Section 2 describes the sample of galaxies, its breakdown into different activity classes, and assesses the quality of the Spitzer-IRS spectra. Section 3 provides the details of our analyses, including the spectral decomposition and modeling. The results and a discussion of their implications are presented in Section 4. The paper is concluded in Section 5 with a summary and conclusions.

2. The Sample

Section 2.1 describes how the sample was obtained, as well as its makeup. This is followed in Section 2.2 with an assessment of the quality of the spectra. Next, in Section 2.3, our method for assigning activity classes is described.

2.1. Spitzer Legacy Programs

Our sample draws from the following five Spitzer Legacy Programs, with data obtained directly from the he NASA/IPAC Infrared Science Archive[4] (IRSA):

1. The Spitzer Infrared Nearby Galaxies Survey (SINGS; Kennicutt et al. 2003). SINGS consists of present-day nearby galaxies ($d < 30$ Mpc), primarily mapping their circumnuclear galactic regions.
2. The Spitzer SDSS GALEX Spectroscopic Survey (SSGSS; O'Dowd et al. 2011). SSGSS consists of normal, star-forming galaxies at $z < 0.2$, color-selected based on the 5.8 μm surface brightness and 24 μm flux.
3. The Spitzer SDSS Statistical Spectroscopic Survey (S5; Schiminovich et al. 2008). S5 is an optically selected statistical sample of star-forming galaxies selected from the SDSS at $z < 0.1$. S5 is an extension of the SSGSS sample over a larger set of SDSS sources and narrower redshift range.
4. The 5 milli-Jansky Unbiased Spitzer Extragalactic Survey (5MUSES; Wu et al. 2010). 5MUSES is a 24 μm flux-limited sample ($f_{24\ \mu m} > 5$ mJy) of intermediate redshift ($\bar{z} \sim 0.144$) designed to bridge the gap between the bright, nearby star-forming galaxies and much fainter, distant sources.
5. The Great Observatories All-Sky LIRG Survey (GOALS; Armus et al. 2009). GOALS consists mostly of low-redshift ($z < 0.09$) Luminous Infrared Galaxies (LIRGs), with a range of interaction stages (major mergers, minor mergers, and isolated galaxies).

The galaxies from these Legacy Programs cover a wide range in M_*, SFR, and Z (Table 1) and sample various activity classes and galaxy environments, such as star-forming galaxies

[3] www.astrochemistry.org/pahdb/
[4] irsa.ipac.caltech.edu

(SFGs) and active galactic nuclei (AGN), which include Seyfert (Sy) and low-ionization nuclear emission-line regions (LINERs), composite systems of combined starburst and AGN contribution (CO), as well as LIRGs at various interaction stages (see Section 2.3). There is a large diversity among the sample in terms of physical environment, as well as distance–which translates to different sizes on the sky and thus differences in the spatially probed regions, i.e., nuclear versus circumnuclear, resolved versus unresolved, etc., and observational parameters. In this work, we do not focus on these differences, but rather examine the average PAH characteristics wholesale, as well as their connection with general galaxy properties.

The galaxy properties were collected from the MPA-JHU catalog[5] or directly from the literature, when available. Table 4 in Appendix 4 provides an overview of the collected properties per Legacy Programs. It must be noted that these properties are not always derived using the same methods/calibrations (we refer the reader to the Legacy Programs themselves for details).

The total number of galaxy spectra considered is 910 and all cover both the SL (5–14.2 μm) and LL (13.9–39.9 μm) segments. In this work, we make use of only the SL segment, which holds all the prominent PAH emission features, as well as as a large number of atomic fine-structure lines and rotational lines from molecular hydrogen. In Paper II, we will examine the impact of utilizing the LL segment in our analysis.

2.2. Quality Assessments

All SL spectra were moved to rest-frame wavelengths (μm) and their signals were put into units of flux density (Jy). The majority of spectra in the sample show prominent PAH emission features. However, there are a few that show very weak or no PAH emission at all. A wide range in dust continua is observed, from relatively weak to dominating the spectrum. In some rare cases, there are apparent calibration issues, which predominantly affect the SL2 (5–7.4 μm) part of the spectrum. Others have been affected by solar flares, causing a large spread in signal-to-noise ratio (S/N) (SSGSS; O'Dowd et al. 2011). For the spectra and details on the data reduction, we refer to the Legacy Programs themselves.

The quality of each spectrum was assessed using the S/N of the total spectrum (S/N_{tot}) and the S/N of the 11.2 μm PAH band ($S/N_{11.2}$). Specifically, we require: (i) $S/N_{tot} > 2.4$, which is the value that corresponds to the fifth percentile, with the median being 9.55; and (ii) $S/N_{11.2} \geqslant 3$, in order to acquire spectra of resolved PAH features. The S/N_{tot} is computed as the ratio of the integral of a spectrum's intensity and uncertainty. $S/N_{11.2}$ is computed with respect to an underlying, straight-line continuum. The flux density (S) of the 11.2 μm PAH band is simultaneously fitted with the sum of a first-order polynomial and a Gaussian line profile between 11.1–11.3 μm. For the noise (N), the uncertainties of the fit were propagated.

2.3. Galaxy Activity Classification

The SEDs of galaxies can show significant variation depending on activity class (e.g., SFGs and AGN), which is also true for their mid-IR spectra. For example, AGN systems show suppressed PAH intensities, a phenomenon that has been related to either PAH destruction (e.g., Smith et al. 2007) induced by the harsh radiation field associated with AGNs, or to the PAH emission being swamped by the AGN continuum (e.g., Armus et al. 2007).

For those galaxies with optical spectroscopic coverage (516 galaxies), we derive their activity classifications following Maragkoudakis et al. (2018a), which uses the combined classification acquired from the three optical emission line diagnostics ([O III]/Hβ—[N II]/Hα, [O III]/Hβ—[S II]/Hα, and [O III]/Hβ—[O I]/Hα; see Baldwin et al. 1981; Kewley et al. 2001; Kauffmann et al. 2003; Kewley et al. 2006; Schawinski et al. 2007) to classify galaxies into SFGs, Sy, LINER, and CO. For the SSGSS, S5, and 5MUSES Legacy data, we used optical spectroscopic information from the MPA-JHU catalog, and for the SINGS galaxies, the optical activity classification was obtained from Moustakas et al. (2010).

An alternative classification scheme using mid-IR spectra takes the equivalent width of the 6.2 μm PAH band ($EQW_{6.2}$ (Armus et al. 2007) to classify galaxies as SFGs, AGN, and CO. Following Armus et al. (2007), we defined star-formation-dominated systems ($\equiv$SFGs) as those having an $EQW_{6.2} > 1.5$ μm, composite systems (both starburst and AGN contributions; $\equiv$CO) as those with $0.2 < EQW_{6.2} \leqslant 0.5$ μm, and AGN-dominated systems as those with $EQW_{6.2} \leqslant 0.2$ μm.

There is 86.3% agreement between the optical and $EQW_{6.2}$ classification, where the Sy and LINERs were considered as AGNs. A typical case for divergence was the classification of Sy as CO when using the $EQW_{6.2}$ method. The $EQW_{6.2}$ method breaks the sample down into 84% SFGs, 10% AGN, and 6% CO.

3. Analysis

The overall data analysis largely follows that described in, e.g., Boersma et al. (2018), and consists of the following five steps.

1. *Isolating the PAH Emission Spectrum*—Emission that originates in PAHs is separated from the underlying stellar and dust continuum, as well as from emission lines associated with molecular hydrogen and atomic species (Section 3.1). The spectra are simultaneously compensated for extinction and PAH band strengths are determined.
2. *Fitting the PAH Emission Spectrum*—The 5.2–14.2 μm SL PAH emission spectrum is fitted using PAHdb, which allows breaking down the emitting PAH family into contributing PAH subclasses, i.e., charge, size, composition, and structure (Section 3.2).
3. *Estimating Uncertainties of PAHdb-derived Parameters*—A Monte Carlo technique is employed to estimate PAHdb uncertainties (Section 3.2.3).
4. *Extrapolating the PAH spectrum*—The fitted PAH spectrum is extrapolated to provide a complete 3–20 μm PAH spectrum (Section 3.2.4).
5. *Calibrating Qualitative PAH Proxies*—The connection between PAH band strength ratios measured from step 1 and the PAH subclass decomposition from step 2 is examined (Section 3.3).

[5] wwwmpa.mpa-garching.mpg.de/SDSS/DR7

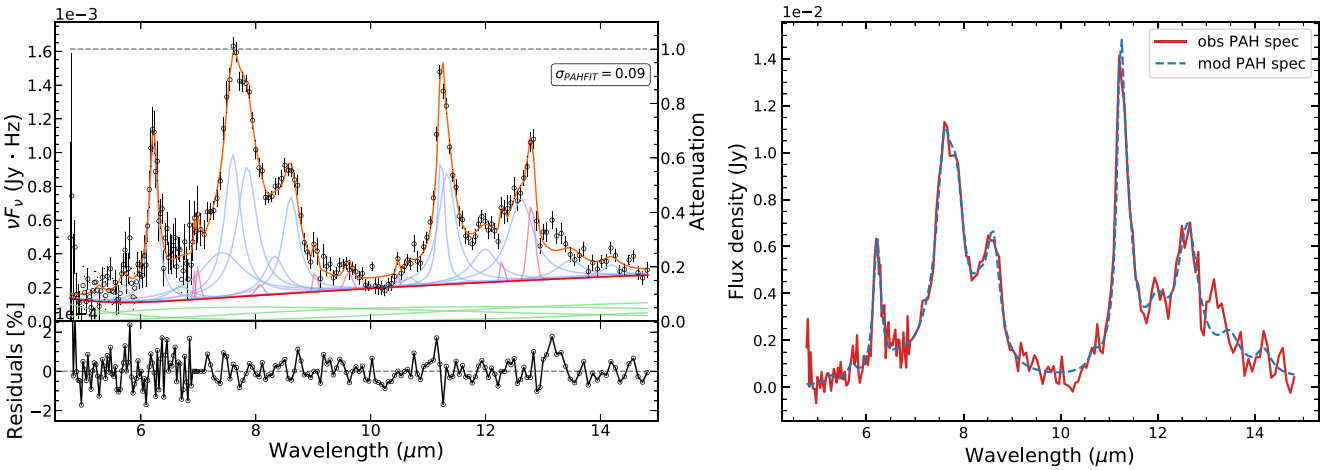

Figure 1. Left: PAHFIT decomposition of the 5.2–14.5 μm Spitzer-IRS spectrum of the galaxy SDSS J093001.33+390242.0 (ID: S5_11_4, in the S5 catalog). The fit (orange line) is synthesized using the following components: Dust features (light blue lines), atomic and H_2 lines (magenta lines), continuum (green lines; the total continuum emission is shown as a red line), and attenuation (dashed black line). $\sigma_{\rm PAHFIT}$ is provided in the box (see Section 3.1) for details. Right: Modeled (blue dashed line) and observed (red line) 5.2–14.5 μm isolated PAH spectrum (see Section 3.1 for details) for the galaxy SDSS J093001.33+390242.0.

3.1. PAHFIT

A 5.2–14.2 μm spectral decomposition was performed with the Python version of PAHFIT.[6] PAHFIT is an Astropy (Astropy Collaboration et al. 2018) affiliated package. The Python version of PAHFIT is based off the IDL version by Smith et al. (2007) and is currently being ported as part of a JWST Early Release Science (ERS) Program (Berné et al. 2022).[7] The reader is referred to Smith et al. (2007) for a description of PAHFIT. A comparison between the results from the IDL and Python versions of PAHFIT is done in Appendix H.

The quality of the spectral decomposition and modeling is assessed in terms of the ratio between the integral of the absolute fit residuals and that of the input spectrum ($\sigma_{\rm pahfit}$). A near-perfect fitted spectrum would result in $\sigma_{\rm pahfit} \sim 0$, with poorer fits yielding higher values.

The left panel of Figure 1 demonstrates the PAHFIT decomposition of the 4.2–14.2 μm spectrum of SDSS J093001.33+390242.0, an SFG from the S5 Legacy program, and has a $\sigma_{\rm pahfit}$ of 0.09, the median value for the entire sample. The fit provides a good separation between the different components with 1%–1.5% residuals that are predominantly at the noise level. For this particular galaxy, the PAHFIT modeled extinction is negligible, while the silicate extinction at 9.7 μm ($\tau_{9.7}$) has a median of 0.1 when considering the entire sample. In the current analysis, only sources with $\tau_{9.7} < 2$ were considered. This constraint was applied to exclude highly attenuated (U)LIRGs from the GOALS sample, for which the PAHFIT decomposition, although producing a low $\sigma_{\rm pahfit}$, may not be optimal, given the difficulty of applying MIR dust models normally used for star-forming and starburst galaxies to heavily obscured LIRGS (see, e.g., Dopita et al. 2011). Additional PAHFIT decomposition examples for various galaxy classes with diverse properties are provided in Appendix A (Figure 10).

The PAHFIT results are used to construct two isolated PAH spectra: (i) the PAHFIT modeled PAH spectrum from combining the different Drude components, and (ii) the observed PAH spectrum from subtracting the dust continuum, stellar continuum, atomic, and H_2 line PAHFIT components from the observed spectrum, and accounting for extinction. It should be noted that both isolated PAH spectra are not independent, as the stellar, dust continuum, and Gaussian components are also used to construct the observed PAH spectrum. However, the observed PAH spectrum retains both emission not matched by any PAHFIT component and the noise. The right panel of Figure 1 compares the two isolated PAH spectra for the galaxy SDSS J093001.33+390242.0.

The figure shows both spectra possessing the salient PAH features, with the residual of the fit shown at the bottom section of the left panel of Figure 1, which are dominated by the noise. However, there are some subtle variances of note. For example, just red of the 12.7 μm PAH band, excess emission is present that resembles a distinct band that is not matched by PAHFIT. Also, some of the galaxy spectra show an 11.2 μm feature that has emission at its blue wing that is not matched by PAHFIT and could be linked to the 11.0 μm satellite feature. Our main analysis relies on the observed (`obs`) PAH spectrum, but the appendices provide an analog analysis for the modeled (`mod`) one.

PAH band strengths, along with the atomic fine structure and rotational line strengths, are determined from PAHFIT. Here, combinations of individual and blended Drude profiles are used to derive strengths for the 6.2, "7.7," 8.6, 11.2, 12.7, 13.5, and 14.2 μm PAH bands, analogous to the IDL version of PAHFIT. To obtain uncertainties for the derived PAH band strengths we have performed Monte Carlo sampling, where the spectra were perturbed 1000 times within their uncertainties and fitted. Subsequently, for each galaxy the statistical average and the standard deviation of each PAH band strength was determined. The PAH band strengths determined this way have been made available online.[8] In Paper II, we will compare and contrast this approach with others for recovering PAH band strength, e.g., the spline method (e.g., Uchida et al. 2000; Hony et al. 2001; Peeters et al. 2002; Galliano et al. 2008; Boersma et al. 2014b; Peeters et al. 2017; Xie et al. 2018).

3.2. PAHdb

The isolated PAH emission spectra obtained from Section 3.1 are further analyzed using PAHdb. Specifically,

[6] github.com/PAHFIT/pahfit

[7] JWST ERS program ID: 1288, pdrs4all.org.

[8] www.astrochemistry.org/pah_galaxy_properties/

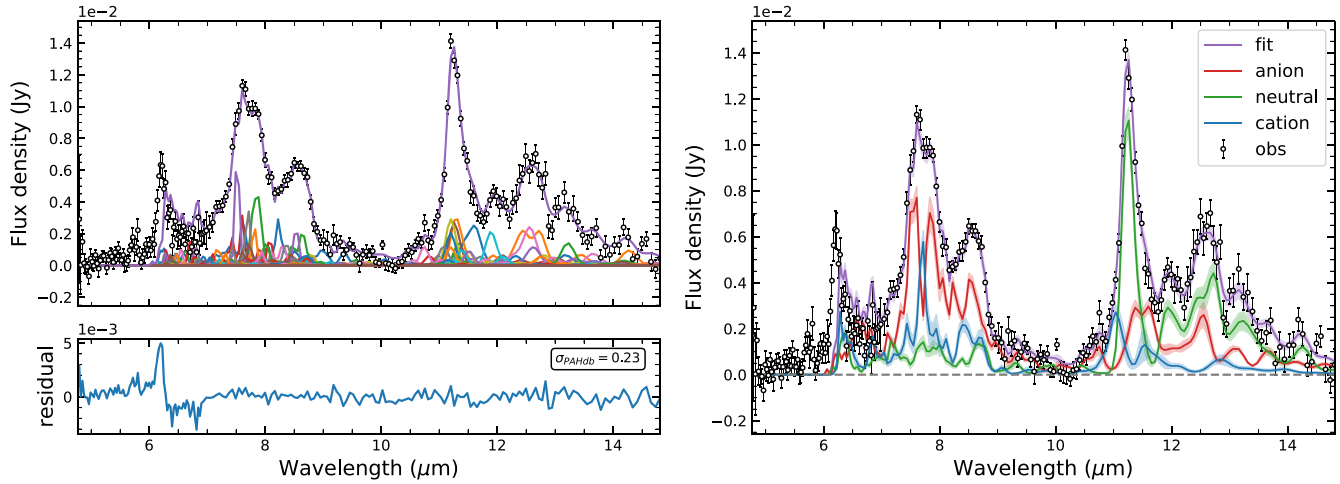

Figure 2. PAHdb fit and charge decomposition of the 5.2–14.5 μm PAH spectrum of the galaxy SDSS J093001.33+390242 (circles). Left: Contribution from each of the 46 individual PAH molecules (colored lines), along with the residual spectrum (bottom panel). The inset shows $\sigma_{\rm PAHdb}$ (see Section 2.2). Right: Breakdown in terms of charge. The uncertainties obtained from the Monte Carlo sampling are shown for each component as a shaded envelope. See Section 3.2.3 for details.

the galaxy PAH spectra are fit utilizing the AmesPAHdb-PythonSuite,[9] which is based off the IDL suite[10] of tools, along with version 3.20 of PAHdb's library of density functional theory (DFT) computed spectra. This library holds 4233 quantum-chemically calculated absorption spectra of PAHs with various structures, charge states, sizes, and compositions. This allows the analysis of astronomical spectra without adopting any ad hoc assumptions regarding the characteristics and state of the underlying PAH population (e.g., Li & Draine 2001), as all the properties of the individual PAH molecules used to synthesize the modeled spectrum can be fully recovered.

3.2.1. The Pool of Astronomically Relevant PAH Spectra in PAHdb

A pool of spectra from PAH molecules that meet the astronomically relevant criteria as laid out in Bauschlicher et al. (2018) are considered. Specifically, PAHs containing more than 20 carbon atoms ($\overline{N_C}$), which are assumed to survive the harsh interstellar environments (e.g., Allamandola et al. 1989; Puget & Leger 1989). Furthermore, either only spectra from "pure" PAHs or those containing nitrogen and no aliphatic side groups are used. Except for fullerenes, the spectra from fully dehydrogenated PAHs are also not considered. The pool thus arrived at contains 2968[11] spectra.

3.2.2. Model Parameters

In order to model the astronomical PAH *emission*, the DFT-computed *absorption* data (see, e.g., Mattioda et al. 2020) need to be converted into *emission* spectra. This requires taking into account: (i) the radiation field that PAHs are exposed to, (ii) the molecular relaxation process after excitation, (iii) the line profile and the width of the emitting bands, and (iv) possible band shifts due to anharmonic effects.

Here, we consider a range of excitation energies, 6, 8, 10, and 12 eV, together with an emission model that takes the entire emission cascade into account (see e.g., Boersma et al. 2011, 2013). Gaussian line profiles are used with an FWHM of 15 $\rm cm^{-1}$. A 15 $\rm cm^{-1}$ redshift is applied to mimic (some) anharmonicity effects, a typical value adopted in the literature (e.g., Bauschlicher et al. 2009). The impact of using different line profiles or omitting a redshift (Mackie et al. 2018) will be explored in Paper II. While the different excitation energies will help to discern any sensitivity to the radiation field, they also accommodate construction of the galaxy PAH emission template spectra (Section 4.4). Our main analysis relies on PAH spectra computed using an excitation of 8 eV.

3.2.3. Fitting, Uncertainties, and Breakdown

The PAHdb fitting was performed using a Non-Negative Least Chi-square minimization approach (NNLC; Désesquelles et al. 2009). Figure 2 (left panel) presents the results of the PAHdb fit of the 5.2–14.5 μm PAH spectrum of the galaxy SDSS J093001.33 + 390242 (the same galaxy as in Figure 1). Overall, the figure shows a good fit. Additional PAHdb fitting and breakdown examples for various galaxy classes with diverse properties are provided in Appendix A (Figure 11).

Similarly as for PAHFIT, PAHdb uncertainties ($\sigma_{\rm PAHdb}$) are quantified as the ratio between the integrals of the absolute residuals over that of the input spectrum (see also Section 3.1). While $\sigma_{\rm pahfit}$ shows a value of 0.09, $\sigma_{\rm PAHdb}$ is considerably larger at 0.23, though that value is on par with those reported elsewhere for similar fits (e.g., Bauschlicher et al. 2018; Ricca et al. 2021).

It has been proposed that this relatively large "error" is driven by PAHdb fits having systematic difficulty in matching certain wavelength regimes (e.g., Bauschlicher et al. 2018). For example, as is apparent in Figure 2, the blue side of the 6.2 μm PAH band is not well-matched. This particular difficulty has been attributed to the limited number of—and variation in—PANHs in PAHdb's libraries. PANHs are, to date, the only PAHs that are able to accommodate the very blue 6.2 μm emission (e.g., Peeters et al. 2002; Hudgins et al. 2005; Ricca et al. 2021). Furthermore, the emission from ∼5–6 μm is attributed to PAH overtone and combination bands (e.g.,

[9] github.com/PAHdb/AmesPAHdbPythonSuite
[10] github.com/PAHdb/AmesPAHdbIDLSuite
[11] The pool can be obtained on the PAHdb website by using the query string "magnesium=0 oxygen=0 iron=0 silicium=0 chx=0 ch2=0 c>20 h>0" and further adding in the fullerenes with UIDs: 717, 720, 723, 735, 736, and 737. Note that the returned pool will be dependent on the version of the library used; here, we use version 3.20.

Boersma et al. 2009), which are not part of the PAH emission spectra modeled here. In Appendix F, we quantify the fraction of the 6.2 μm PAH band recovered by PAHdb with respect to that recovered by PAHFIT.

To gain a better understanding of these systematics and for a fairer quality criterion, we turn to computing σ_{PAHdb} for wavelength ranges that bracket the main PAH features. For SDSS J093001.33+390242, these are 1.02, 0.57, 0.04, 0.04, 0.05, 0.1, and 0.1 for $\sigma_{5.2}$, $\sigma_{6.2}$, $\sigma_{7.7}$, $\sigma_{8.6}$, $\sigma_{11.2}$, $\sigma_{12.0}$, and $\sigma_{12.7}$, respectively. These values indicate that indeed much of the "error" is systematic in nature. The median $\sigma_{,\mathrm{PAHdb}}$ for the entire sample is 0.3, while that for $\sigma_{\mathrm{PAHdb,11.2}}$ is 0.07, a value on par with that found for σ_{pahfit}.

Although the identification of individual astronomical PAH molecules in the mid-IR is (practically) impossible due to band overlap, PAHdb fits do allow probing the general state of the PAH population in terms of subclasses. It has been shown that the PAH charge and size composition can be determined with a high degree of reliability (e.g., Andrews et al. 2015). In turn, they can be tied to the PAH ionization fraction and PAH size distribution.

To obtain uncertainties for the derived parameters, we turn to a Monte Carlo (MC) approach. Here, the observed PAH spectra are perturbed 1000 times within their uncertainties and fitted. Subsequently, for each galaxy the statistical average and the standard deviation are determined.

The right panel of Figure 2 shows the PAHdb-fitted 5.2–14.5 μm PAH spectrum of SDSS J093001.33+390242.0 again, but now broken down in terms of charge. The figure shows a small amount of variation for the fit itself, with somewhat more for the three charge components (anion, neutral, and cation) individually.

From the PAHdb fits, we construct a PAH size distribution. Here, we take a PAH's effective radius (in Å) as $a_{\mathrm{eff}} = \sqrt{A/pi}$, where A is the area of the PAH computed by multiplying the sum of the number of rings by the area of a single (3–8 member) ring. Subsequently, a power law is fitted and the power-law index (α) is recorded. Besides α, we also record the average PAH size in terms of number of carbon atoms (N_{C}), the two-charge state PAH ionization fraction ($f_{\mathrm{i}} \equiv n_{\mathrm{PAH}^+}/(n_{\mathrm{PAH}^0} + n_{\mathrm{PAH}^+})$), and the different hydrogen adjacency classes, all with their associated Monte Carlo–determined uncertainties.

3.2.4. Extrapolating the Fitted PAH Spectrum

JWST is anticipated to provide a wealth of spectroscopic information from 0.6 to 28.8 μm. Consequently, acquiring information that spans this entire range is valuable for gaining early insights as well as benchmarking JWST observations. Therefore, we extrapolated the PAHdb-fitted PAH spectra to cover the 3–20 μm range.

Furthermore, information gained with regard to the 3.3 μm PAH band would be of value for non-high-redshift Spitzer observations (Sajina et al. 2009), where the band is absent. The intensity of 3.3 μm PAH emission is particularly sensitive to PAH size. When ratioed to the 11.2 μm PAH band strength, it provides a robust tracer of PAH size (Allamandola et al. 1989; Schutte et al. 1993; Mori et al. 2012; Ricca et al. 2012; Croiset et al. 2016; Maragkoudakis et al. 2018b, 2020). In addition, the 3.3 μm PAH band can place tight constraints on the total energy put into PAHs in dust models (e.g., Lai et al. 2020).

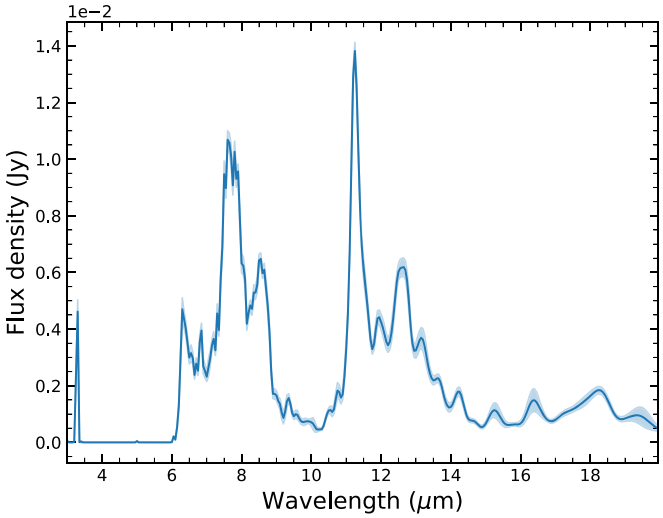

Figure 3. The extrapolated 3–20 μm PAH spectrum (blue line) of the galaxy SDSS J093001.33+390242.0, with the associated uncertainty shown as the shaded envelope. See Section 3.2.4 for details.

Moreover, extrapolated spectral data beyond 15 μm would be of use for those Spitzer-IRS observations that lack LL data.

The extrapolated spectra are synthesized by co-adding the 3–20 μm spectra of each PAH contributing to a fit, where each PAH spectrum has been multiplied by its fitted weight. Since this is done as part of the Monte Carlo sampling, the final extrapolated spectrum is accompanied by uncertainties. Figure 3 presents the extrapolated 3–20 μm spectrum of the galaxy SDSS J093001.33+390242.0. The figure reveals a distinct, simple 3.3 μm PAH band, as well as substantial substructure longward of 15 μm. Note that the astronomical 3.3 μm feature is due to highly energetic C–H stretching modes that couple overtone and combination bands, and it is bracketed with more structure than the harmonic band shows in Figure 3 (Mackie et al. 2018; Maltseva et al. 2018). Thus, the actual structure of any astronomical 3.3 μm PAH feature will differ substantially from that shown in the figure. The strength of the extrapolated 3.3 μm PAH band is determined by fitting a Gaussian.

3.3. Calibrating Qualitative PAH Proxies

PAH band strength ratios are sensitive to, and therefore reflect, astrophysical conditions. For example, the coupled C–C stretching and C–H in-plane bending modes increase considerably upon ionization, compared to C–H stretching modes (e.g., Allamandola et al. 1999), and thus the 6.2/11.2 and 7.7/11.2 μm PAH band strength ratios are frequently used to measure the PAH ionization balance, and subsequently—via empirical calibrations—the ionization parameter γ ($\equiv (G_0/n_{\mathrm{e}})(T_{\mathrm{gas}}/1\ \mathrm{K})^{0.5}$) (e.g., Bregman & Temi 2005; Galliano et al. 2008).

The PAHdb decomposition quantifies the cation and neutral PAH contribution, which allows for a *quantitative* calibration of the empirical, *qualitative* proxies used to probe variations in the properties of the emitting PAH populations, such as charge, size, or structure. For example, the PAH charge balance is often approximated as:

$$\frac{n_{\mathrm{PAH}^+}}{n_{\mathrm{PAH}^0}} \propto \frac{I_{6.2}}{I_{11.2}}, \quad (1)$$

(see Boersma et al. 2014b, 2016, 2018) where the PAH cation and neutral densities ($n_{\rm PAH^+}$ and $n_{\rm PAH^0}$, respectively) are obtained from the PAHdb decomposition. When assuming two accessible ionization states and parameters applicable for circumcoronene[12] ($C_{54}H_{12}$), which is considered representative of an average interstellar PAH ($N_{\rm C} = 50$–100; Croiset et al. 2016), the PAH ionization parameter can be expressed as:

$$\gamma \equiv (G_0/n_{\rm e})(T_{\rm gas}/1\ {\rm K})^{0.5} = 2.66\left(\frac{n_{\rm PAH^+}}{n_{\rm PAH^0}}\right)[\times 10^4\ {\rm cm^3}]. \quad (2)$$

Similarly, the correlation between the $11.2/3.3\,\mu$m PAH band strength ratio and $N_{\rm C}$ has been well-documented in the literature (e.g., Ricca et al. 2012; Croiset et al. 2016; Maragkoudakis et al. 2020).

4. Results and Discussion

We now investigate the distributions of the derived PAH properties (Section 4.1), correlations among the derived PAH properties, and correlations with galaxy properties, broken down per galaxy activity class (Section 4.3). PAH band strength ratio calibrations are examined in Section 4.2. A library of template galaxy PAH emission spectra, quantified based on $\overline{N_C}$ and $\overline{f_i}$, are presented in Section 4.4. Finally, we discuss some of the limitations associated with our methodology in Section 4.5.

During our analysis, a number of parameters were established to assess the quality of the data and the reliability of the fitting results. We combine these now in such a way as to establish three quality classes: Q1–Q3. All three classes meet the spectral quality requirements that $S/N_{\rm (tot)} \geqslant 2.4$ and $S/N_{\rm (11.2)} \geqslant 3$ (Section 2.2). Each subsequent class sets less stringent constraints on the PAHFIT uncertainty ($\sigma_{\rm pahfit}$; Section 3.1), and the PAHdb uncertainty ($\sigma_{\rm PAHdb,11.2}$; Section 3.2.3). For $\sigma_{\rm pahfit}$ and $\sigma_{\rm PAHdb,11.2}$, the limits are set based on where their cumulative distributions hit 68, 95, and 99.7%. This sets $\sigma_{\rm pahfit} \leqslant 0.11$, 0.27 and 0.38, and $\sigma_{\rm PAHdb,11.2} \leqslant 0.07$, 0.12, and 0.26, for Q1, Q2, and Q3, respectively. Q1 has 386, Q2 698, and Q3 778 galaxy spectra. These quality classes provide different levels of confidence and can help with interpreting the results. Our main results are based on Q2 data. A comparison between results derived using the different quality classes is provided in Appendix D. All data have been made available online[13] (see Appendix G).

4.1. PAH Property Distributions

From the PAHdb MC sampling analysis of each galaxy, we collected a set of PAH properties, including $N_{\rm C}$, $f_{\rm i}$, PAH composition ("pure" versus nitrogen containing), and hydrogen adjacency classes information (solo, duo, trio, quartet). A weighted average is computed using the inverse MC-determined uncertainties squared as weights. Figure 4 presents the distributions for $\overline{N_{\rm C}}$, $\overline{f_{\rm i}}$, and the power-law index $\overline{\alpha}$ from the size distribution fits. The number of bins and the bin widths for each histogram are determined using Knuth's rule (Knuth 2006), which utilizes a Bayesian model and computes the posterior probability of the number of bins for a given data set without making any a priori assumptions on the data. Each distribution was also fitted with a Gaussian model for comparison. Besides this, the statistical mean, standard deviation, and skewness were also determined. The results are summarized, alongside the parameters derived from the Gaussian distributions, in Table 2.

The statistical mean and standard deviation for $\overline{N_C}$, $\overline{f_i}$, and $\overline{\alpha}$ distributions are in good agreement with those obtained from the Gaussian modeling, indicating a normal distribution. The weighted average number of carbon atoms is $\overline{N_C} = 55$, with a range of $44 \leqslant \overline{N_C} \leqslant 77$. This average supports the choice of circumcoronene in Section 3.3 and provides confidence for the inferred ionization fraction. The weighted average ionization fraction has a value $\overline{f_i} = 0.37$, with a range of $0.09 \leqslant \overline{f_i} \leqslant 0.81$. For the mean power-law index of the PAH size distribution, a value of $\overline{\alpha} = -1.75$ and a range of $-4.35 \leqslant \overline{\alpha} \leqslant -0.48$ are found.

$\overline{N_C}$ is for all galaxies (taking the standard deviation into account) close to the characteristic value that separates small from large astrophysical PAHs ($N_{\rm C} \simeq 50$; e.g., Tielens 2008). Considering the diversity and mixture of galactic environments, even within a given galaxy, it is, on the one hand, expected that in regions with high radiation field intensity (or hardness) such as star-forming regions or the central regions of AGN hosts, $N_{\rm C}$ will be higher as smaller PAHs are more effectively destroyed. On the other hand, studies on the Small Magellanic Cloud (SMC) (Sandstrom et al. 2010; Sandstrom et al. 2012) suggest that in low-metallicity environments PAHs only form inside dense molecular clouds, and are therefore typically smaller, or that larger PAHs form less efficiently. Consequently, in both scenarios small PAHs are formed that are more susceptible to destruction. Our derived value for $\overline{N_C}$ indicates that the average PAH population in galaxies consists of middle-sized PAHs. Figuring out whether this is the result of smoothing between regions of low- and high-$N_{\rm C}$ PAH populations or something else will require spatially resolved studies within galactic environments.

For $\overline{f_i}$, we find a value of 0.37, indicating an average distribution of ~40% ionized—60% neutral of the PAH population within galaxies. In regions without much ionizing radiation (e.g., interarm diffuse ISM regions), PAHs would be mostly neutral, whereas in regions with high levels of ionization (e.g., PDRs associated with star-forming regions), PAHs are expected to be mostly ionized. The electron recombination rate depends on electron density, which is known to vary on both galaxy-wide and H II-region scales (e.g., Herrera-Camus et al. 2016; Kewley et al. 2019). As such, the mostly average neutral PAH population found for our sample is likely the result of averaging the ionization fraction of a number of regions with different physical conditions.

The average PAH size distribution is weighted toward smaller PAHs, with $\overline{\alpha} \simeq -1.75$. Often, PAHs are considered the extension of grain size distribution into the molecular domain. Compared to the MRN (Mathis et al. 1977; $\alpha = -3.5$) grain size distribution, that of PAHs is less heavily weighted toward smaller PAHs. One possible explanation for this could be that dust grains can grow continuously, whereas PAHs only grow in discrete steps, i.e., one ring at a time.

Breaking down the distributions for $\overline{N_C}$, $\overline{f_i}$, and $\overline{\alpha}$ per activity class (SFG, AGN, and CO) provides no new insights,

[12] Note that there is some uncertainty associated with the parameters used. This uncertainty depends on the adopted electron recombination rates, where the difference between the classical and measured rates on very small PAHs can be as high as nearly an order of magnitude (see Tielens 2005).

[13] www.astrochemistry.org/pah_galaxy_properties/

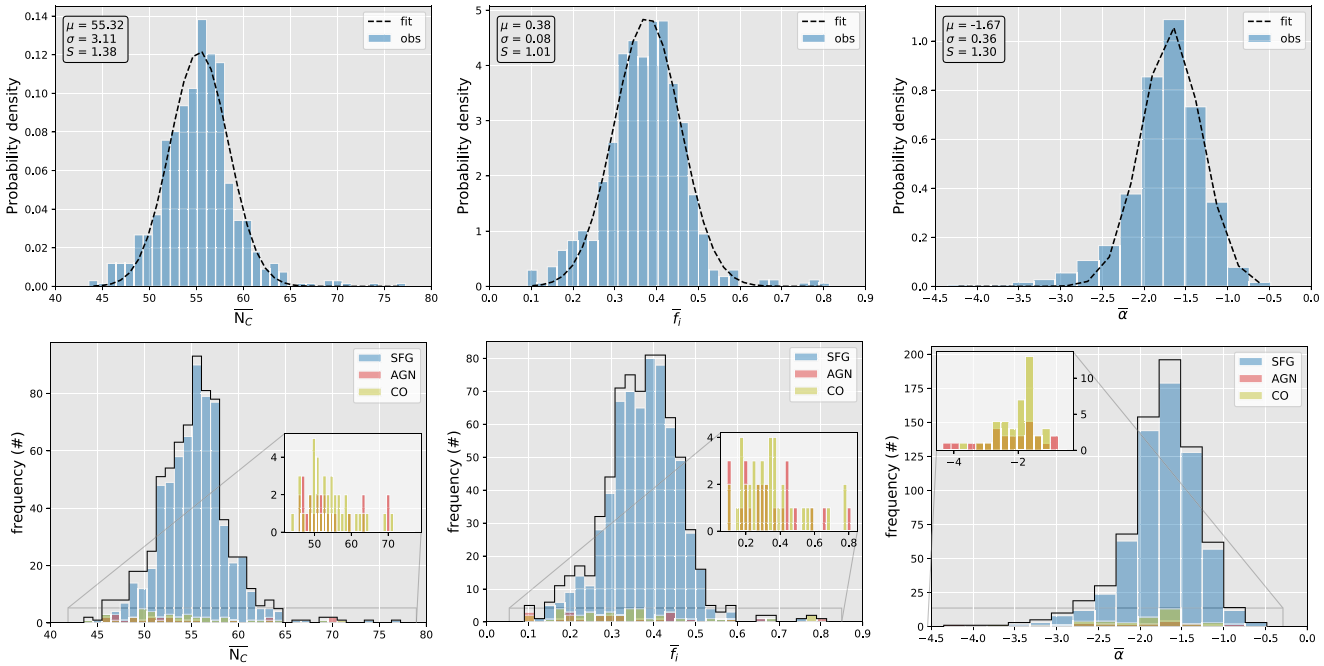

Figure 4. Distributions for the average number of carbon atoms ($\overline{N_C}$; left panels), average ionization fraction ($\overline{f_i}$; middle panels), and average power-law index of the PAH size distribution ($\overline{\alpha}$; right panels). Top row: Probability density distributions fitted with a Gaussian model (black dashed lines). The statistical mean (μ), standard deviation (σ), and skewness (S) are given in the boxes. Bottom row: Probability density distributions broken down by galaxy activity class (SFGs, AGN, and CO). Those of the combined classes are shown in black.

Table 2
PAH Property Distribution Attributes

Parameter	$\mu \pm \sigma$	$\mu_{\rm fit} \pm \sigma_{\rm fit}$ [a]	S [b]
$\overline{N_C}$	55.24 ± 3.90	55.32 ± 3.10	1.39
$\overline{f_i}$	0.37 ± 0.09	0.38 ± 0.08	1.01
$\overline{\alpha}$	-1.75 ± 0.46	-1.67 ± 0.36	1.31
Class	$\overline{N_C}$ $(\mu \pm \sigma)$	$\overline{f_i}$ $(\mu \pm \sigma)$	$\overline{\alpha}$ $(\mu \pm \sigma)$
SFGs	55.38 ± 3.55	0.38 ± 0.08	-1.71 ± 0.41
AGN	53.75 ± 7.08	0.34 ± 0.18	-2.22 ± 0.92
CO	53.87 ± 5.93	0.32 ± 0.15	-2.00 ± 0.56

Notes. Statistical mean (μ) and standard deviation (σ) of the PAH property distributions for all the galaxies (top) and their respective activity classes (bottom).
[a] Mean ($\mu_{\rm fit}$) and standard deviation (σ_{fit}) from Gaussian fit.
[b] Skewness (S).

though this could change when more sources, evenly spread among the different classes, are added.

Recently, Silva-Ribeiro et al. (2022) used PAHdb to study the main type of PAH molecules and the local physical conditions of their irradiating sources in 12 galaxies, where the entire PAHdb library was employed. They concluded that PAH species containing 10–82 carbon atoms were the most abundant in their sample and the PAH population can contain up to 95% of small species and 79% of neutral PAHs, with molecules such as $C_{52}H_{18}$, $C_{10}H_9N$, and $C_{14}H_{11}N$ being present in more than 75% of their sample, while removal of these molecules produced a worsening of the fit. However, inclusion of the entire PAHdb library of molecules can bias the results. In Section 3.2.1, we stressed the importance of considering a pool of PAH(db) molecules that meet astronomically relevant criteria, such as the consideration of only molecules containing more than 20–30 carbon atoms, which can survive destruction via photodissociation.

4.2. PAH Band Strength and PAHdb-derived Correlations

Figure 5 presents the correlations between the PAHdb-derived PAH ionization parameter and PAH size measures versus their well-known PAH band strength ratio proxies, i.e., the $6.2/11.2\,\mu$m and $3.3/11.2\,\mu$m PAH band strengths respectively. Although the $7.7/11.2$ and $8.6/11.2\,\mu$m PAH band strength ratios, which also probe PAH ionization, show a correlation with γ (Appendix C, Figure 14), the $6.2/11.2$—γ correlation is the tightest (Table 3). The correlation is also evident when examining the respective samples; the SSGSS and GOALS samples show even tighter correlations, with respective Pearson's correlation coefficients of $r_{xy} = 0.79$ and $r_{xy} = 0.75$. This relation allows for the estimation of the average ionization parameter within galaxies, directly from observationally measured quantities. Recovering these correlations for both PAH size and charge gives us confidence in the overall PAHdb decomposition (Boersma et al. 2013).

Figure 6 extends the correlation presented in Figure 5 for the $6.2/11.2\,\mu$m PAH band strength ratio versus γ by including data on the reflection nebula NGC 7023 from Boersma et al. (2018). The figure shows what appears to be a continuous transition from the galaxy to NGC 7023 data. To explore this further, three linear fits were performed: (i) for the galaxy and NGC 7023 data combined, (ii) the galaxy and NGC 7023 data combined up to $\gamma = 3 \times 10^4$ cm^3, and (iii) for the NGC 7023 data alone. For cases (i) and (iii), the fitted lines are very comparable, whereas they differ in case (ii).

Per Tielens (2005), the γs for the galaxies fall between that of the general ISM and PDRs. Compared to the correlation found in (Boersma et al. 2018; their Figure 13), the galaxies overlap with the data on M17. Though M17 is classified as an H II region, the data mostly reflects the shielded, more benign

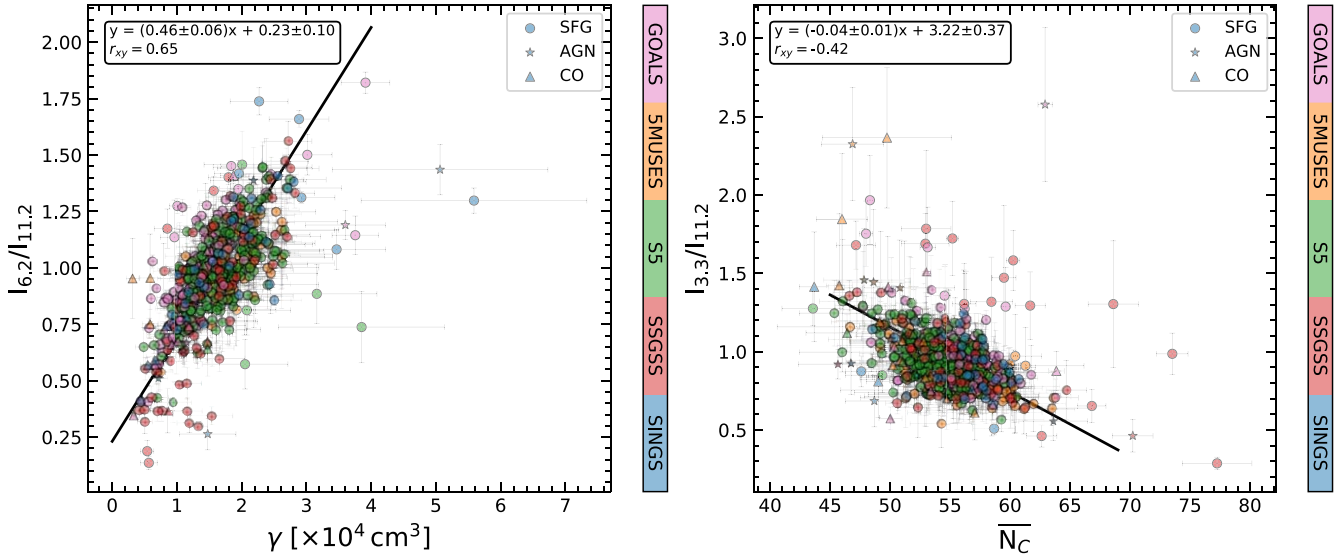

Figure 5. Left: The 6.2/11.2 μm PAH band strength ratio vs. the PAH ionization parameter ($\equiv\gamma$; Equation (2)). Right: The 3.3/11.2 μm PAH band strength ratio vs. $\overline{N_C}$. SFGs are shown as circles, AGN as stars, and COs as triangles. Data points are color-coded based on their associated Legacy program. The linear fits are shown in black and the fit equations are given in the box, together with their Pearson's correlation coefficients (r_{xy}).

Table 3
Correlation and Fit Parameters

Relation	r_{xy}	α	β
6.2/11.2—γ	0.65	0.46 ± 0.06	0.23 ± 0.10
7.7/11.2—γ	0.53	1.29 ± 0.23	1.46 ± 0.36
8.6/11.2—γ	0.38	0.15 ± 0.03	0.48 ± 0.05
3.3/11.2—$\overline{N_C}$	−0.42	−0.04 ± 0.01	3.22 ± 0.37
γ—M_*	−0.36	−0.39 ± 0.06	5.57 ± 0.59
6.2/11.2—sSFR	0.49	0.16 ± 0.01	2.25 ± 0.13
7.7/11.2—sSFR	0.40	0.99 ± 0.08	13.15 ± 0.78
8.6/11.2—sSFR	0.39	0.24 ± 0.03	3.17 ± 0.28
12.0/11.2—duo/solo	0.34	0.20 ± 0.02	0.002 ± 0.025
6.2/7.7—$\overline{N_C}$	−0.17	−0.005 ± 0.001	0.553 ± 0.078

Note. Pearson's correlation coefficient (r_{xy}), slope (α), and intercept (β) values of the linear fits for the various relations between PAH band strength ratios, PAHdb-derived parameters, and galaxy parameters.

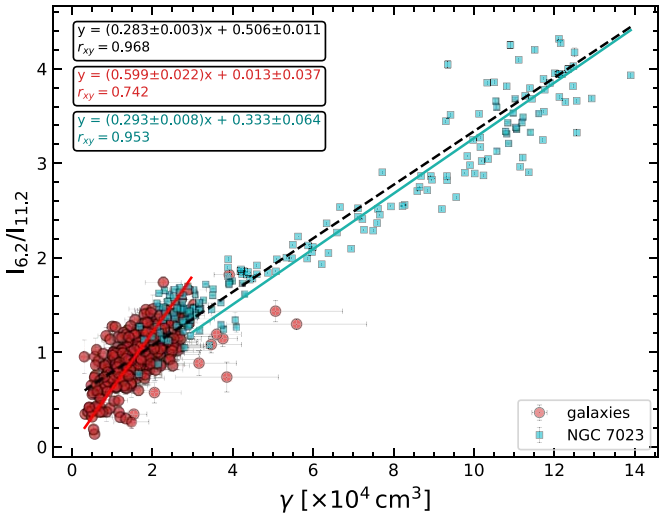

Figure 6. The 6.2/11.2 μm PAH band strength ratio versus the PAH ionization parameter ($\equiv\gamma$; Equation (2)), for galaxies (red circles) and the reflection nebula NGC 7023 (cyan squares). Linear fits are shown for the galaxy and NGC 7023 data (black dashed line), the galaxy and NGC 7023 data up to $\gamma = 3 \times 10^4$ cm^3 (red line), and NGC 7023 data alone (cyan line). The equations are shown with corresponding colors in the boxes, together with their Pearson's correlation coefficients (r_{xy}).

region behind the PDR. Indeed, this ISM-like environment might be more representative of the *average* one encountered in star-forming galaxies, i.e., the bulk of galaxies considered here, as the PDRs associated with H II regions are typically only a sliver on the sky compared to the molecular clouds that house them.

The correlation of the 3.3/11.2 μm PAH band strength with N_C is demonstrated for the galaxy samples (Figure 5, right panel) confirming the effectiveness of the 3.3/11.2 μm PAH band strength ratio as a PAH size indicator in galaxies (Maragkoudakis et al. 2020), and further demonstrating the efficiency of extrapolating the PAHdb-fitted spectra to include the 3.3 μm band. For the 5MUSES and S5 samples, correlations are even tighter, with respective values of $r_{xy} = -0.59$ and $r_{xy} = -0.55$. No correlation was found between the 6.2/7.7 μm PAH band strength ratio–previously employed for PAH size determination (e.g., Draine & Li 2001), with N_C ($r_{xy} = -0.17$; see Table 3 and Appendix C, Figure 14).

A rather weak trend is observed for the 12.0/11.2 μm PAH band strength ratio versus the PAHdb-determined duo-to-solo hydrogen adjacency ratio (Appendix C, Figure 14, and Table 3). The 11.2 and 12.0 μm PAH bands are typically associated with CH out-of-plane bending modes of solo and duo hydrogens, respectively. Therefore, the 12.0/11.2 μm PAH band strength ratio is often employed as a probe for PAH geometry, as solo modes are associated with long straight molecular edges, whereas duo and trio modes correspond to corners (Hony et al. 2001; Tielens 2008). All pairwise relationships between PAH band strength ratios with PAHdb-derived (and galaxy) properties are presented in Appendix B (Figures 12 and 13).

4.3. PAH and Galaxy Properties

We examined possible correlations between the PAHdb-derived PAH properties and galaxy properties. Though weak

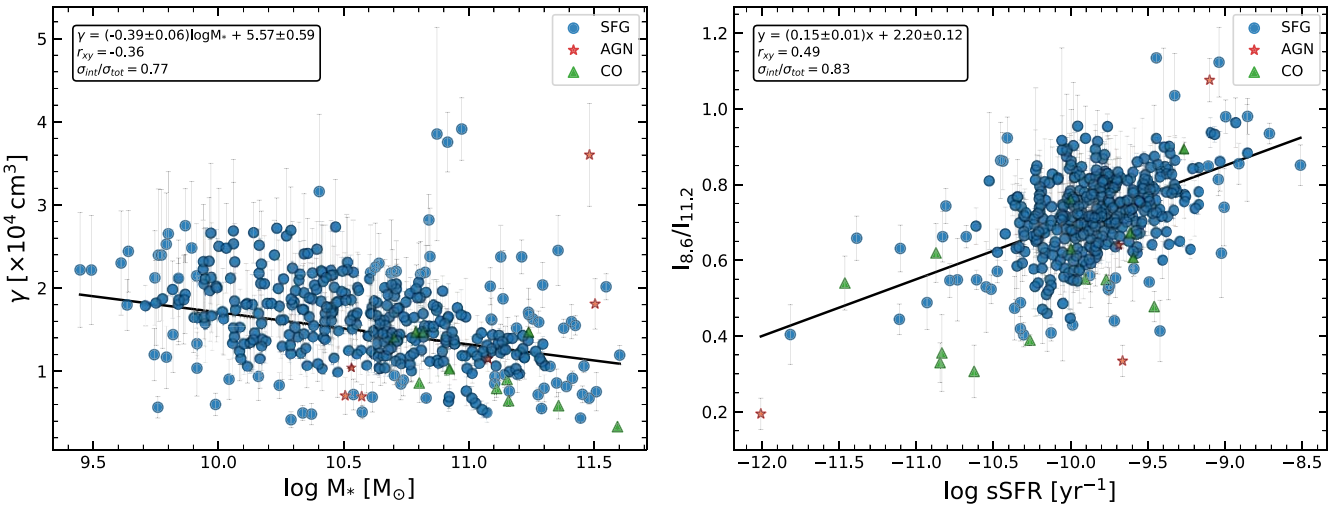

Figure 7. Left: The PAH ionization parameter γ (Equation (2); Section 3.3) vs. stellar mass. Right: The 8.6/11.2μm PAH band strength ratio vs. sSFR. SFGs are shown as circles, AGN as stars, and CO as triangles. The black line shows the linear fit when assuming the presence of intrinsic scatter. The found fit equation is given in the box, together with the Pearson's correlation coefficient (r_{xy}), and the ratio of the intrinsic to the total scatter ($\sigma_{\rm int}/\sigma_{\rm tot}$).

($r_{\rm xy} = -0.36$), one possible (anti-)correlation was found between M_* and γ, which is presented in Figure 7 (left panel). Assuming such a correlation exists, we introduce an intrinsic scattering term per Williams et al. (2010) and find that it accounts for 77% ($\sigma_{\rm int}/\sigma_{\rm tot}$) of the total scatter. A possible origin for the large intrinsic scatter is the large variation in how the observations were acquired between the different Legacy programs, e.g., fiber or slit-spectroscopy, whether only nuclear- or circumnuclear material or the galaxy as a whole was observed. The presence of such a correlation would support the view that, in low-mass and low-metallicity galaxies, the radiation field of young massive stars can more efficiently ionize PAHs, due to the lower amounts of opacity and attenuating material (dust grains, gas and metals), whereas in more massive and metal-rich systems of higher column density material, the UV radiation of young stars is subjected more to attenuation, resulting in lower PAH ionization fractions. This (anti-)correlation becomes tighter when examining the Q1 quality class case ($r_{xy} = 0.53$; see Appendix D).

A moderate correlation is identified between the PAH band strength ratio proxies of the PAH ionization (i.e., $I_{6.2}/I_{11.2}$, $I_{7.7}/I_{11.2}$, $I_{8.6}/I_{11.2}$) and the specific SFR (sSFR $\equiv$ SFR/M_*), with $I_{8.6}/I_{11.2}$—sSFR (Figure 7, right panel) being the tightest ($r_{xy} = 0.49$; Table 3), with the intrinsic scatter accounting for the 83% of the total scatter. While the sSFR describes the relative SFR per galaxy stellar mass—and thus per atomic hydrogen (H I) mass content (e.g., Catinella et al. 2010; Maddox et al. 2015), the inverse of sSFR defines a timescale for the formation of the stellar population of a galaxy, where lower sSFR corresponds to older stellar populations for a constant or single-burst star formation history (Whitaker et al. 2017). In this sense, the correlation between the PAH ionization proxies with sSFR yields the increase of PAH ionization in systems of younger stellar populations and more recent star formation episodes.

Figure 8 presents a pairwise comparison between galaxy and PAHdb-derived parameters. A similar comparison between PAH band strength ratios and galaxy parameters is given in Appendix B. The figure shows that well-documented relations, like that between SFR and M_* (i.e., the galaxy main sequence; Brinchmann et al. 2004; Elbaz et al. 2007; Whitaker et al. 2012; Maragkoudakis et al. 2017; Sánchez 2020; Ellison et al. 2021) and the M_*–metallicity relation (MZ relation; e.g., Tremonti et al. 2004), are present. However, no *obvious* correlation is found between the galaxy and PAHdb-derived parameters, other than the tentative one described between γ and M_*, and similarly that of the PAH band strength ratios with sSFR (Figure 12).

PAH luminosity has been successfully calibrated as a tracer of SFR in galaxies (e.g., Calzetti et al. 2007; Shipley et al. 2016; Maragkoudakis et al. 2018b) and is commonly used as such. The cause for there being no correlation between the SFR and any of the PAH band strength ratios or PAHdb-derived parameters could be twofold: (i) the derived SFR is highly sensitive to the choice of calibrator, as different wavelengths tend to trace different stellar populations, different galaxy components, and different environments, and each calibrator has its own systematic effects and biases (e.g., Calzetti et al. 2010; Murphy et al. 2011; Cluver et al. 2017; Mahajan et al. 2019; Kouroumpatzakis et al. 2021; Xie & Ho 2022); and (ii) the makeup of the PAH population between galaxies is largely homogeneous (Andrews et al. 2015).

To put these results on a stronger footing, a selection of (multiple) homogeneous subsamples, broken down and grouped based on their physical conditions and environments (e.g., morphology, dust content, etc.), probing regions that are similar (e.g., in terms of distance and size), with properties established using similar methods (calibrations), would be required.

4.4. Library of Template PAH Emission Spectra for Galaxies

We have created a library of PAH emission spectra that can be used as templates in, e.g., galaxy SED modeling. The templates are parameterized on $\overline{N_C}$ and $\overline{f_i}$, which are are the average of each extrapolated galaxy spectrum in each 2D bin. Figure 9 compares a number of template spectra at fixed $\overline{N_C}$ and varying $\overline{f_i}$ (left), and vice versa (right). At fixed $\overline{N_C}$, the PAH features in the 6–9 μm wavelength range increase with increasing $\overline{f_i}$, whereas the 3.3 μm PAH band and those between 11–13 μm decrease. At fixed $\overline{f_i}$, the 3.3 μm PAH band and those between 11–13 μm increase with increasing $\overline{N_C}$, with no

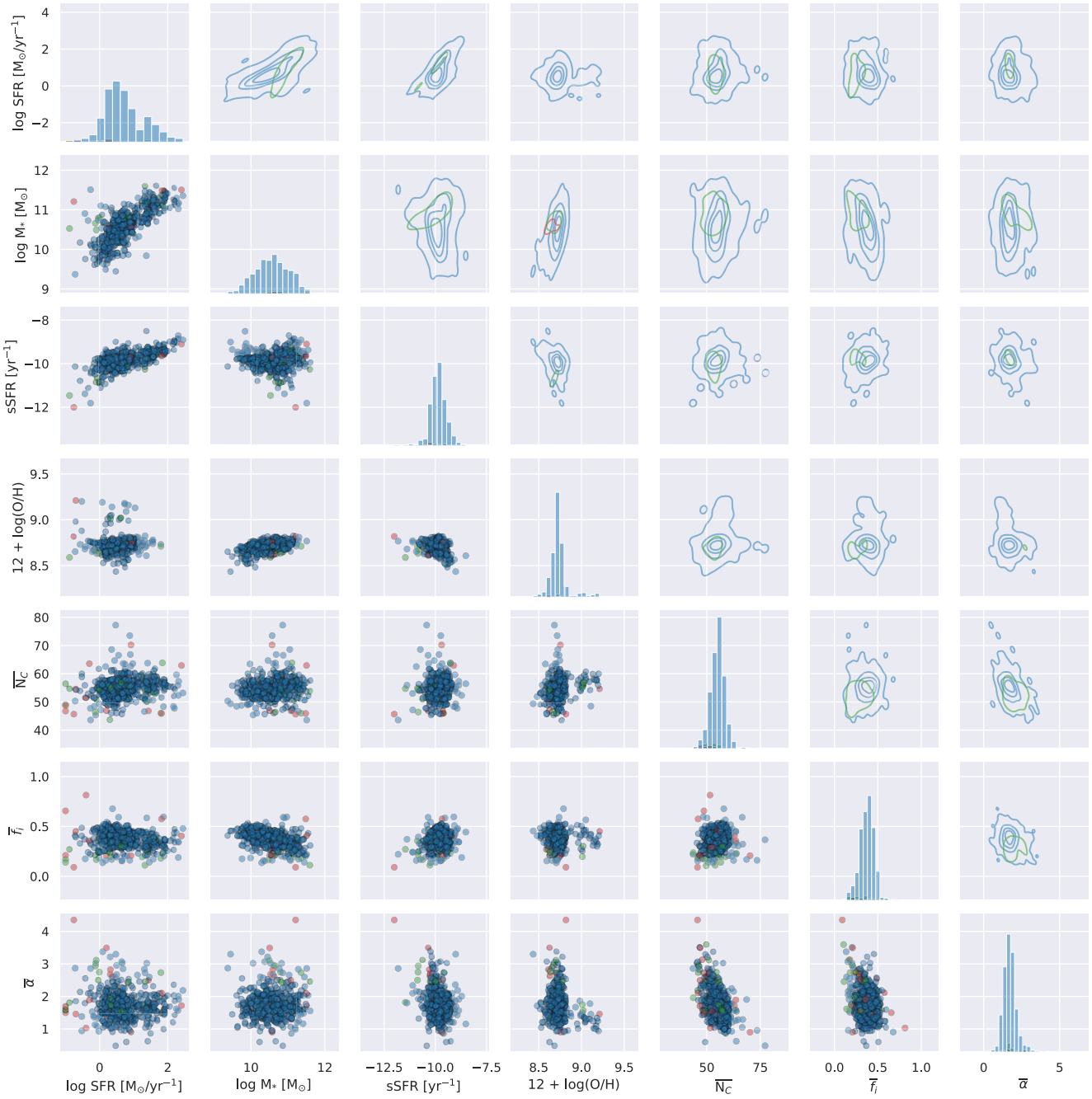

Figure 8. Pairwise relationships of galaxy (SFR, M_*, sSFR, and 12+log(O/H)) and PAH ($\overline{N_C}$, $\overline{f_i}$, and $\overline{\alpha}$) properties (points), along with their respective distributions (histograms), and kernel density estimations (contours at five levels, corresponding to isoproportions of the probability mass density, i.e., contours at 80%, 60%, 40%, and 20%). Colors correspond to galaxy activity classes, with SFGs shown in blue, AGN in red, and CO in green.

substantial variation between 6–9 μm. The templates are offered for different radiation fields (6, 8, 10, and 12 eV) and have been made available online.[14]

4.5. Final Thoughts

The results presented in this work depend strongly on the models, algorithms, and tools used to decompose the galaxy spectra, as well as the spectral resolution and quality of the astronomical spectra themselves.

With respect to PAHFIT, the resulting isolated PAH emission spectra, and subsequently the measured band strengths, are dependent on the adopted extinction model (i.e., fully mixed or a foreground screen of dust), as well as the shape of the extinction curve, which can vary in between galaxies (Salim & Narayanan 2020). Boersma et al. (2018) showed that the choice of extinction curve can have a significant impact on the measured PAH band strength ratios for H II regions. Specifically, they noted that PAHFIT-like fits appear sensitive to the shape of the used extinction curve through its interplay with other components of the spectra. That work showed that analyzing Spitzer spectral cubes using the $R_V = 5.5$ extinction curve from Weingartner &

[14] www.astrochemistry.org/pahdb/templates_gal/

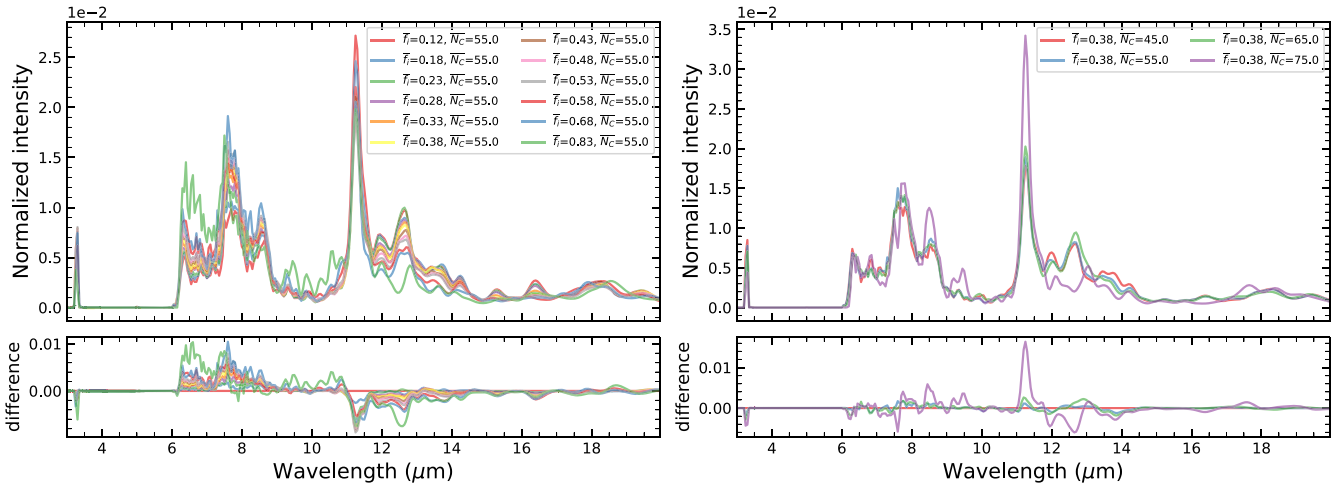

Figure 9. PAHdb-derived PAH emission templates. Left: Templates at fixed $\overline{N_C}$ and varying $\overline{f_i}$. Right: Templates at fixed $\overline{f_i}$ and varying $\overline{N_C}$. The spectra have been normalized (in F_ν units) on the total integrated flux. The bottom panels show the spectral differences between templates by subtracting each spectrum from the first spectrum in the set.

Draine (2001) results in visual extinction (A_V) maps with large pixel-to-pixel variations and discontinuities. However, when moving to the extinction curve from Chiar & Tielens (2006), a smooth continuous map is obtained. Subsequently, the choice of extinction curve impacts the derived PAH band strengths as well, which can be significant (up to ∼40%). In addition, PAHFIT has been trained on star-forming and starburst galaxies, and the application to heavily obscured galaxies here did not yield reliable results.

PAHdb holds continuously growing libraries of quantum-chemically computed and laboratory-measured PAH spectra and evolving fitting tools. The results presented here are based on version 3.20 of PAHdb's library of DFT-computed harmonic spectra. Regarding library content, it is important to understand its incompleteness. Efforts are underway to address this issue, specifically in matching the 6.2 μm and the detailed structure of the 10–15 μm region. Furthermore, the inclusion of anharmonicity in the computation of PAH emission spectra will help resolve any ambiguity with regard to applying a 15 cm^{-1} redshift and the need for PAH anions to accommodate the extended red wings of the PAH bands (e.g., Bregman & Temi 2005; Bauschlicher et al. 2009).

In addition to the considerations described above and the current completeness state of PAHdb, putting forward a list of distinct dominant PAH molecules responsible for the galaxy PAH spectra would be premature, and as such, it is avoided here. A comprehensive examination and quantification of degeneracies for robust conclusions on the dominant PAH populations in galaxies will be explored in Paper II, along with the sensitivity of the results to PAH emission parameter choices.

The analysis and results presented in this work predominantly encapsulate the behavior of SFGs, as they make up a considerable fraction of the galaxies in the Legacy Programs. Nonetheless, the current representation of the AGN and CO classes in the Legacy programs show similar distributions for the properties of their PAH populations to that of SFGs (Section 4.1).

5. Summary and Conclusions

We have performed a detailed analysis of the PAH component of over 900 Spitzer-IRS spectra from galaxies with different nuclear activity classes, utilizing the data, models, and tools provided through PAHdb. The main conclusions from our work are summarized below.

(i) The PAH population within galaxies consists of middle-sized PAHs with an average number of carbon atoms of $\overline{N_C} = 55$ and does not show much variation across the different activity classes (SFGs, AGN, and CO). The average two-level PAH ionization fractions found are $\overline{f_i} = 0.37$, $\overline{f_{i(\mathrm{SFG})}} = 0.38$, $\overline{f_{i(\mathrm{AGN})}} = 0.33$, and $\overline{f_{i(\mathrm{CO})}} = 0.33$.

(ii) PAH band strength ratios commonly used as proxies for the charge state of the PAH population are successfully calibrated against the PAH ionization parameter, which allows for an estimate of the average ionization parameter in galaxies directly from observations. Furthermore, the correlation for the 6.2/11.2 μm PAH band strength ratio and γ naturally extends that found for the RN NGC 7023 to lower γ.

(iii) A moderate correlation is found between the 8.6/11.2 μm PAH ratio and sSFR, indicating an increase of PAH ionization in systems of younger stellar populations and recent star formation episode, and a weak anticorrelation is observed for the PAH ionization parameter ($\equiv\gamma$) and M_*, which suggests a higher ionization efficiency for PAHs in low-mass galaxies. This could point to a slightly different makeup of the PAH population, i.e., formation and evolution pathways, depending on M_*.

(iv) The 3.3/11.2 μm PAH band strength ratio, commonly used as a proxy for PAH size, is successfully calibrated against $\overline{N_C}$. Here, the 3.3 μm PAH band strength is determined from extrapolating the PAHdb fits to cover the bands.

(v) A library of PAH emission spectral templates parameterized on average excitation energy, $\overline{N_C}$, and $\overline{f_i}$ are provided.

We would like to thank the referee for providing constructive comments and suggestions that have improved the clarity of this paper. A.M.'s research was supported by an appointment to the

NASA Postdoctoral Program at NASA Ames Research Center, administered by the Oak Ridge Associated Universities through a contract with NASA. C.B. is grateful for an appointment at NASA Ames Research Center through the San José State University Research Foundation (NNX17AJ88A). C.B., J.D.B., and L.J.A. acknowledge support from the Internal Scientist Funding Model (ISFM) Directed Work Package at NASA Ames titled: "Laboratory Astrophysics—The NASA Ames PAH IR Spectroscopic Database." We are grateful to the PAHFIT developers Karl Gordon, Thomas Lai, Alexandros Maragkoudakis, Els Peeters, Bethany Schefter, Ameek Sidhu, and J.D. Smith. Usage of the Metropolis HPC Facility at the Crete Center for Quantum Complexity and Nanotechnology of the University of Crete, supported by the European Union Seventh Framework Programme (FP7- REGPOT-2012-2013-1) under grant agreement no. 316165, is also acknowledged.

Appendix A
Examples of Decomposition and Modeling for Galaxy Spectra of various Properties

Figure 10 presents PAHFIT decomposition examples of spectra from different galaxy classes (SFG, AGN, and starburst) and properties (metallicity and morphological type). For the different classes, a main-sequence SFG, an AGN verified in both optical (BPT) and $EQW_{6.2}$ activity diagnostics, and a starburst of SFR $> 100\ M_{\odot}/$ yr were selected. Metallicity examples were drawn from galaxies with metallicity estimates of similar methods (i.e., the MPA-JHU catalog). Examples of different galaxy morphology were drawn from the SINGS sample with available morphological classifications. Similarly, PAHdb charge breakdowns for the same galaxies, based on their MC sampling modeling, are presented in Figure 11.

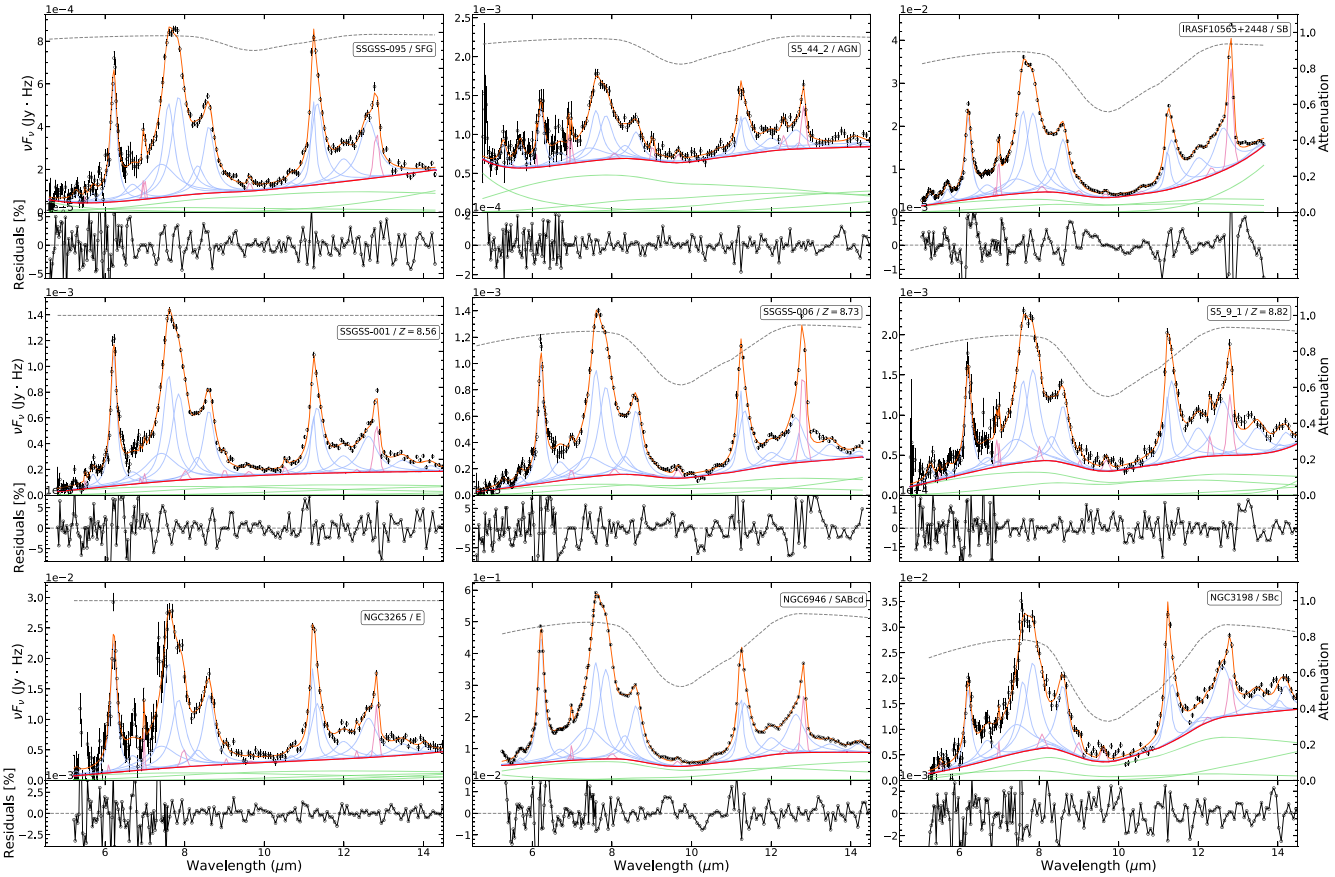

Figure 10. PAHFIT decomposition of spectra from different galaxy classes and properties. Top row: A main sequence SFG (left), an AGN (middle), and a starburst galaxy (right). Middle row: Spectra at different metallicities; $Z = 8.56$ (left), $Z = 8.73$ (middle), and $Z = 8.82$ (right). Bottom row: Different morphological types; Elliptical (left), SABcd (middle), and SBc (right). See Figure 1 for the color coding.

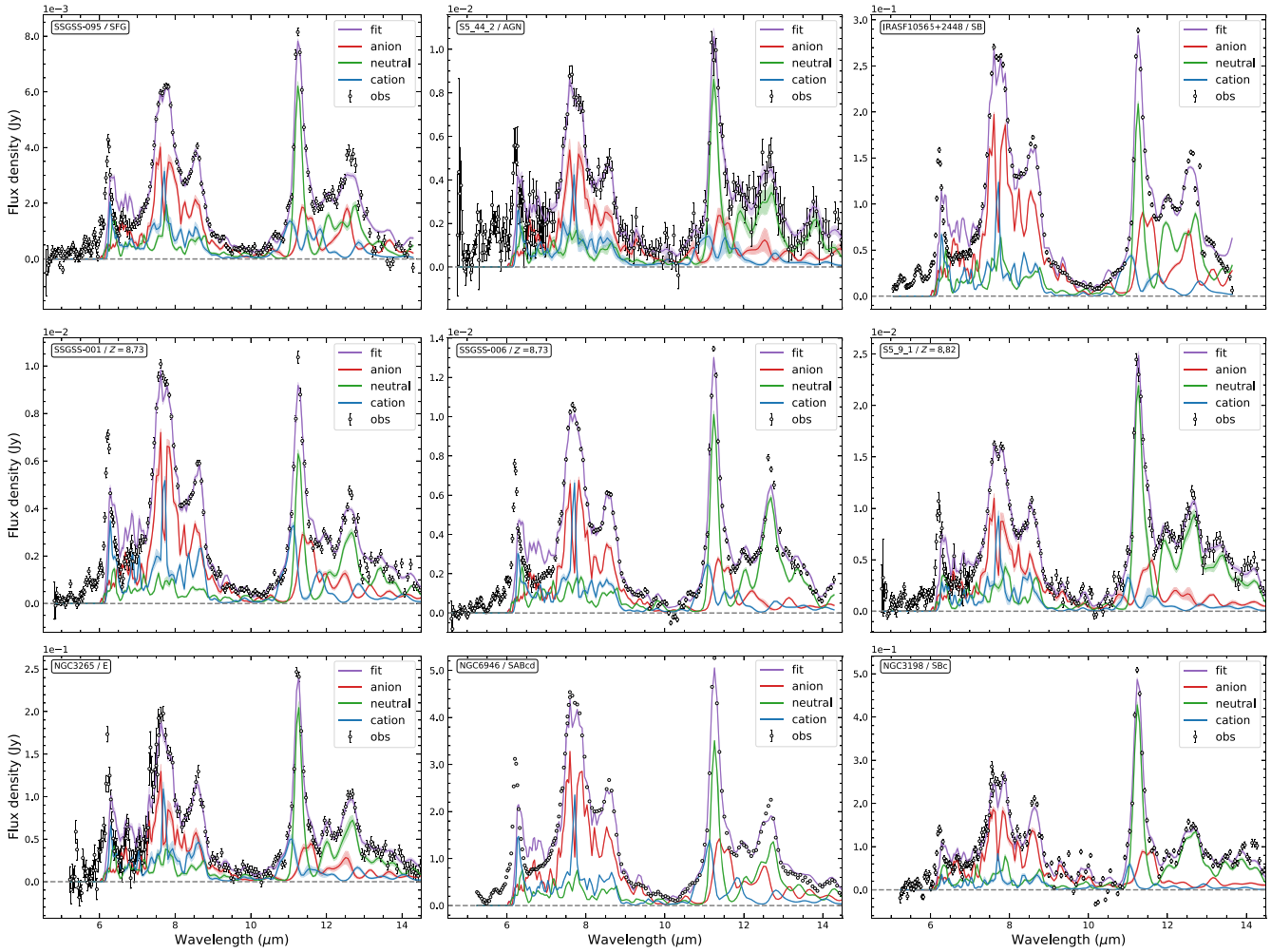

Figure 11. PAHdb charge breakdown of spectra from different galaxy classes and properties. Top row: A main sequence SFG (left), an AGN (middle), and a starburst galaxy (right). Middle row: Spectra at different metallicities; $Z = 8.56$ (left), $Z = 8.73$ (middle), and $Z = 8.82$ (right). Bottom row: Different morphological types; Elliptical (left), SABcd (middle), and SBc (right).

Appendix B
Relationship between PAH Band Strength Ratios with Galaxy and PAHdb Properties

Figures 12 and 13 present the pairwise relationship between PAH band strength ratios ($I_{6.2}/I_{11.2}$, $I_{7.7}/I_{11.2}$, $I_{8.6}/I_{11.2}$, and $I_{3.3}/I_{11.2}$) with galaxy properties (SFR, M_*, sSFR, and 12+log (O/H)) and PAHdb-derived properties ($\overline{N_C}$, $\overline{f_i}$, and $\overline{\alpha}$), respectively.

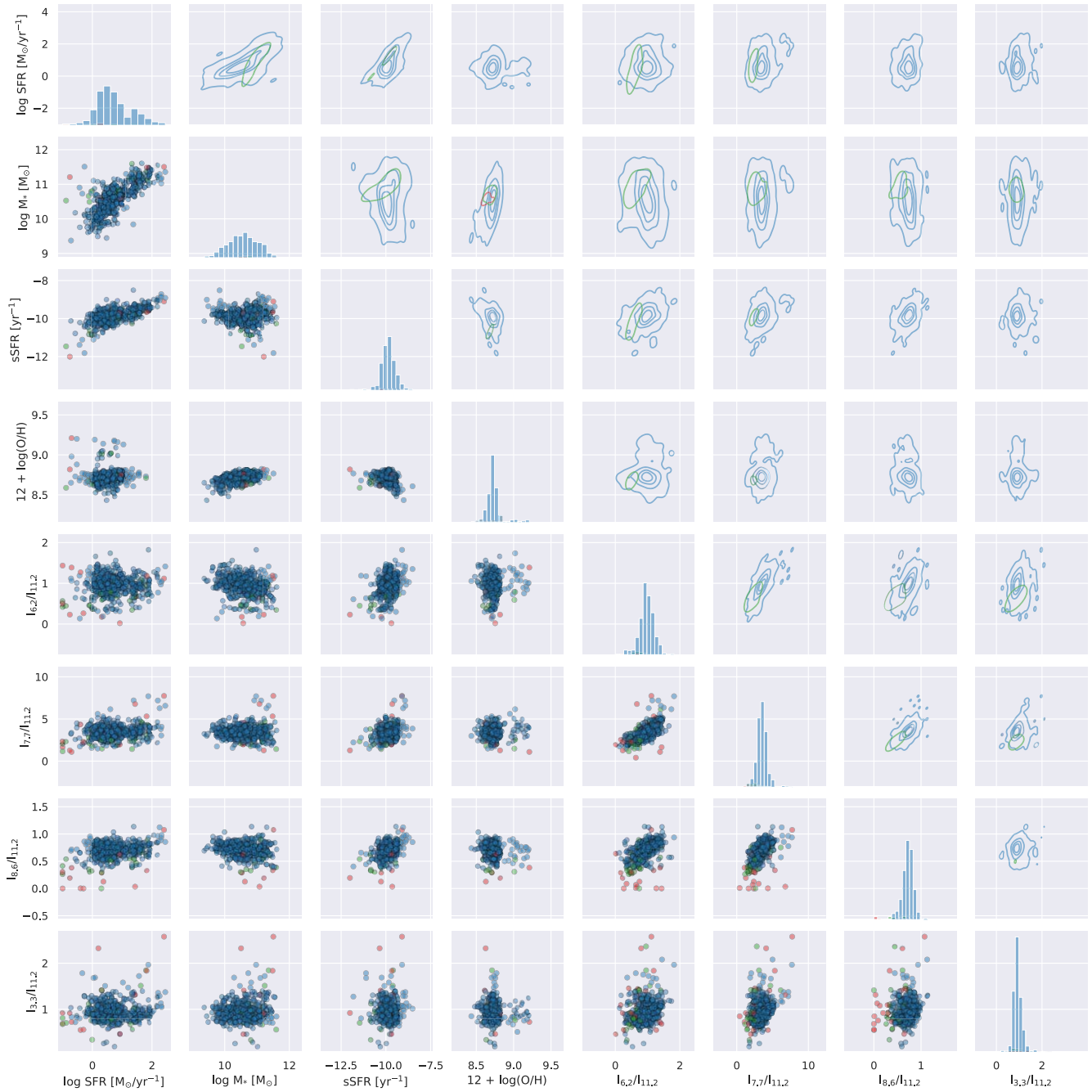

Figure 12. Pairwise relationships of PAH band strength ratios ($I_{6.2}/I_{11.2}$, $I_{7.7}/I_{11.2}$, $I_{8.6}/I_{11.2}$, and $I_{3.3}/I_{11.2}$) and galaxy (SFR, M_*, sSFR, and 12+log(O/H)) properties (points), along with their respective distributions (histograms), and kernel density estimations (contours at five levels, corresponding to isoproportions of the probability mass density, i.e., contours at 80%, 60%, 40%, and 20%). Colors correspond to galaxy activity classes, with SFGs shown in blue, AGN in red, and CO in green.

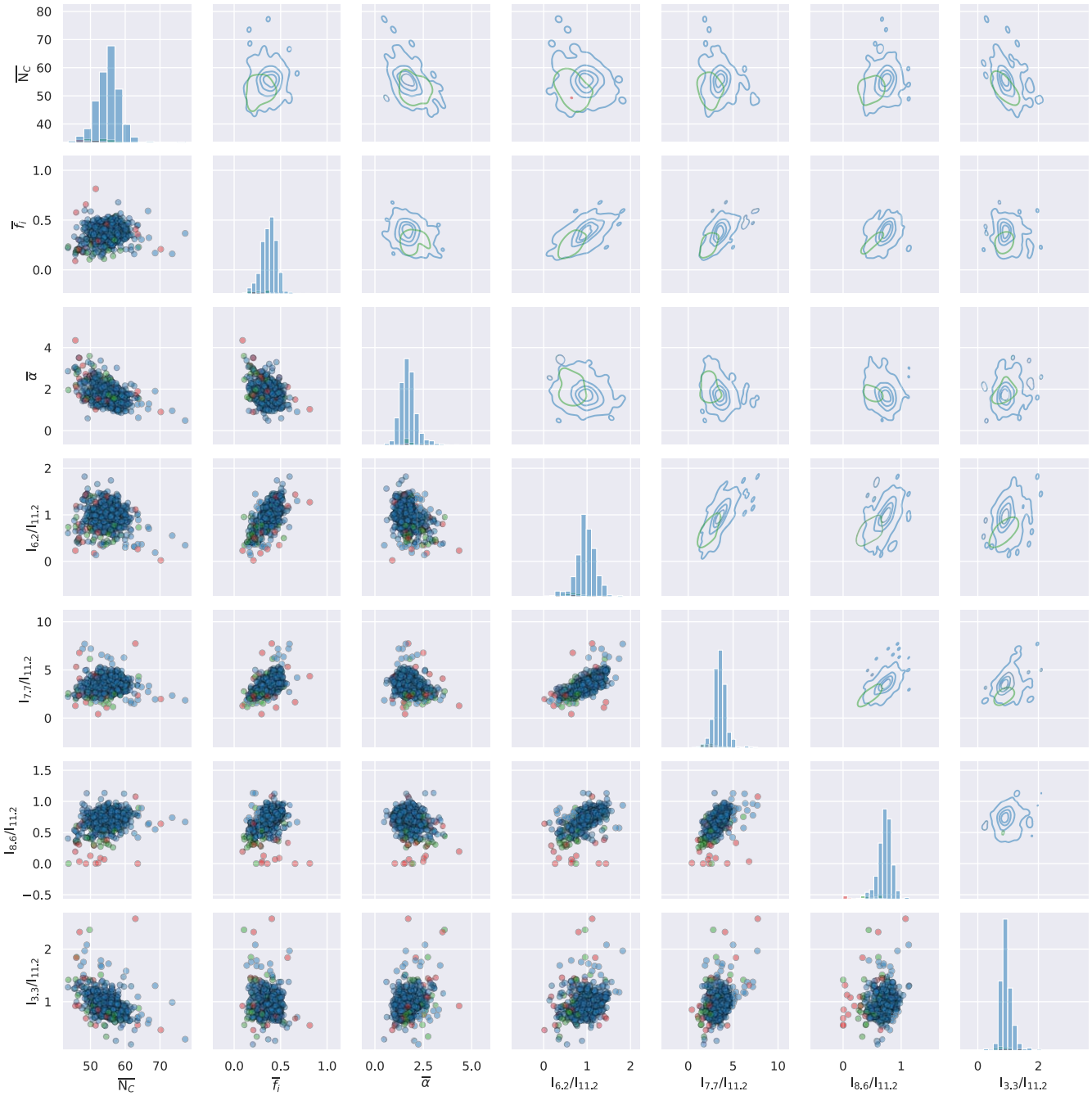

Figure 13. Pairwise relationships of PAH band strength ratios ($I_{6.2}/I_{11.2}$, $I_{7.7}/I_{11.2}$, $I_{8.6}/I_{11.2}$, and $I_{3.3}/I_{11.2}$) and PAH ($\overline{N_C}$, $\overline{f_i}$, and $\overline{\alpha}$) properties (points), along with their respective distributions (histograms), and kernel density estimations (contours at five levels, corresponding to isoproportions of the probability mass density, i.e., contours at 80%, 60%, 40%, and 20%). Colors correspond to galaxy activity classes, with SFGs shown in blue, AGN in red, and CO in green.

Appendix C
Weak or Absent Correlations

Figure 14 presents the relationship between PAH band strength ratios and PAHdb-derived parameters with weak or absent correlations. See also the discussion in Section 4.2.

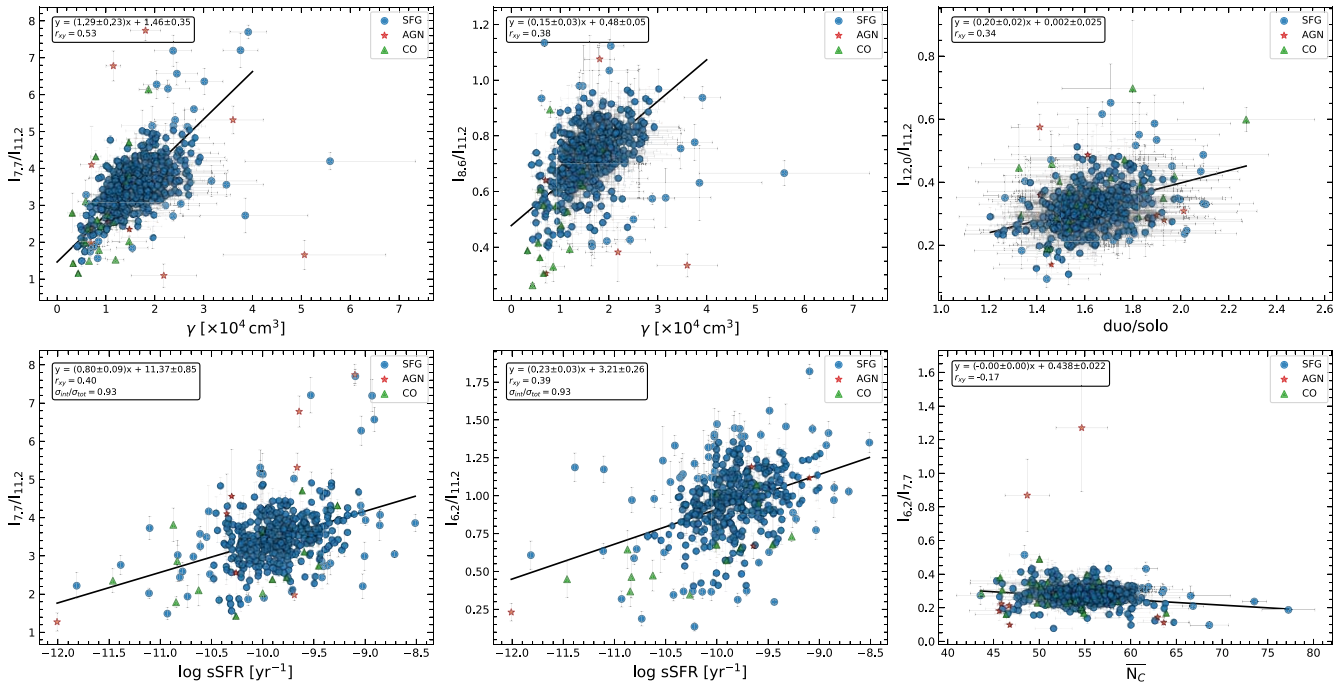

Figure 14. Relationship between PAH band strength ratios and PAHdb-derived parameters showing weaker or no correlations. Top left: $I_{7.7}/I_{11.2}$ vs. γ. Top middle: $I_{8.6}/I_{11.2}$ vs. γ. Top right: $I_{12.0}/I_{11.2}$ vs. duo/solo. Bottom left: $I_{7.7}/I_{11.2}$ vs. sSFR. Bottom middle: $I_{6.2}/I_{11.2}$ vs. sSFR. Bottom right: $I_{6.2}/I_{7.7}$ vs. $\overline{N_C}$. The fit equations are given in the box, together with the Pearson's correlation coefficient (r_{xy}), and the ratio of the intrinsic to the total scatter ($\sigma_{\rm int}/\sigma_{\rm tot}$) where present.

Appendix D
Comparison between Quality Classes

Three quality classes were defined (Q1–Q3; see Section 4), with Q1 being the most restrictive. Figure 15 presents the correlation between γ and M_*, the $6.2/11.2\,\mu$m PAH band strength ratio with γ, and the $3.3/11.2\,\mu$m PAH band strength ratio with $\overline{N_C}$ for Q1 and Q3. Those for Q2 are presented in Figures 7 and 5. The anticorrelation between γ and M_* improves when going to Q1 ($r_{xy} = -0.53$). Similarly, there is a tighter correlation between the $6.2/11.2\,\mu$m PAH band strength ratio and γ for Q1 ($r_{xy} = 0.73$). The correlation for the $3.3/11.2\,\mu$m PAH band strength ratio and $\overline{N_C}$ is well-established and shows no real differences between the different quality classes.

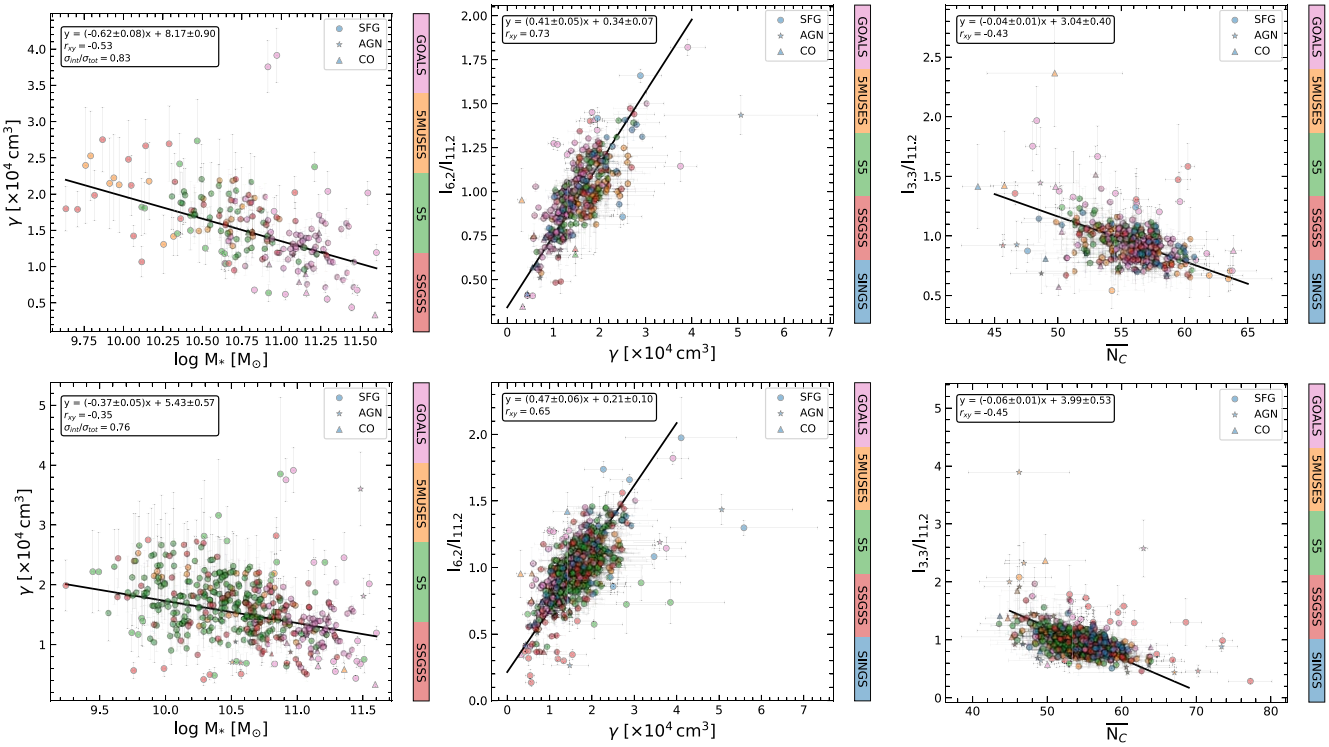

Figure 15. Correlations for γ and stellar mass (left panels), the $6.2/11.2$ μm PAH band strength ratio and γ (middle panels), and the $3.3/11.2$ μm PAH band strength ratio and $\overline{N_C}$ (right panels) for the Q1 (top row) and Q3 (bottom row) quality classes. SFGs are shown as circles, AGN as stars, and CO as triangles. Data points are color-coded based on their associated Legacy program. The linear fit is shown as the black line and the fit equation is given in the legend, together with the Pearson's correlation coefficient (r_{xy}), and the ratio of the intrinsic to the total scatter ($\sigma_{\rm int}/\sigma_{\rm tot}$) where present.

Appendix E
Types of PAH Spectra

E.1. Observed versus Modeled Isolated PAH Spectrum

Two types of isolated PAH spectra have been considered: (i) The PAHFIT modeled PAH spectrum, and (ii) that constructed by subtracting the PAHFIT dust continuum, stellar continuum, atomic, and H_2 line components from the observed spectrum, and accounting for extinction. Figure 16 compares $\overline{N_C}$ and $\overline{f_c}$ for the two spectral types.

The figure shows that using either type of isolated PAH spectrum gives, within the uncertainties, consistent results. Each method has its benefit. For example, the isolated observed PAH spectrum retains residual PAH emission that is not matched by any of the PAHFIT components. On the other hand, for low-S/N spectra, the modeled PAH spectrum will be able to reconstruct some of the band structures of individual features (Boersma et al. 2016).

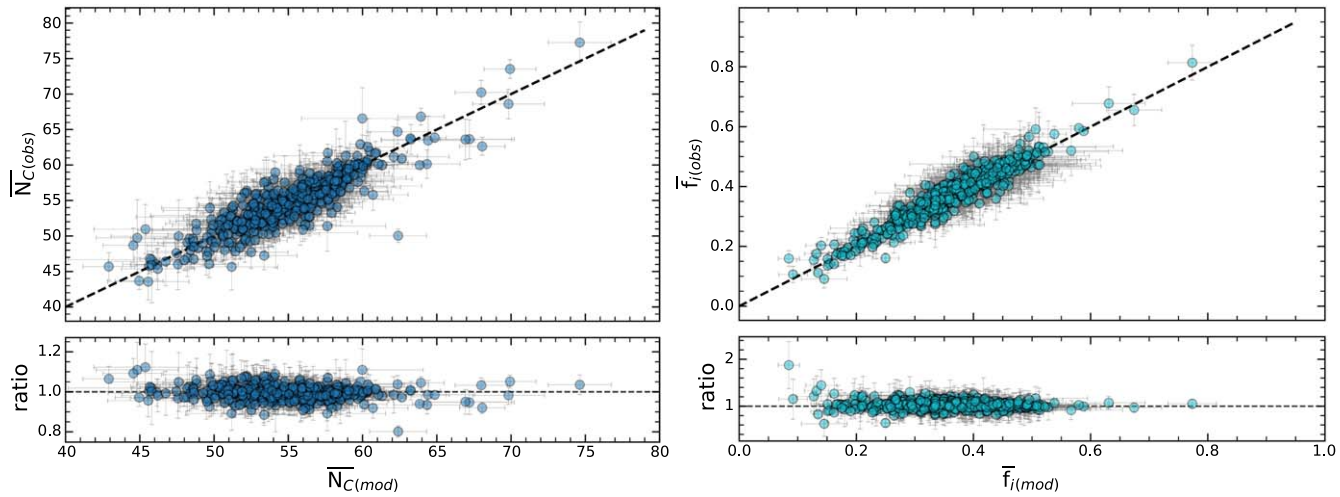

Figure 16. Comparison between $\overline{N_C}$ (left panel) and $\overline{f_i}$ (right panel) derived from the observed and modeled isolated Q2 PAH spectrum. The dashed line is the line of equality. In the bottom panels, the two derived quantities are ratioed.

E.2. Radiation Fields

Figure 17 presents the distribution of the PAHdb derived properties $\overline{N_C}$, $\overline{f_i}$, and $\overline{\alpha}$ for the three other excitation energies considered; 6, 10, and 12 eV. $\overline{N_C}$ and $\overline{fi}$ show a small shift toward lower values with increasing photon energy but remain consistent within their uncertainties.

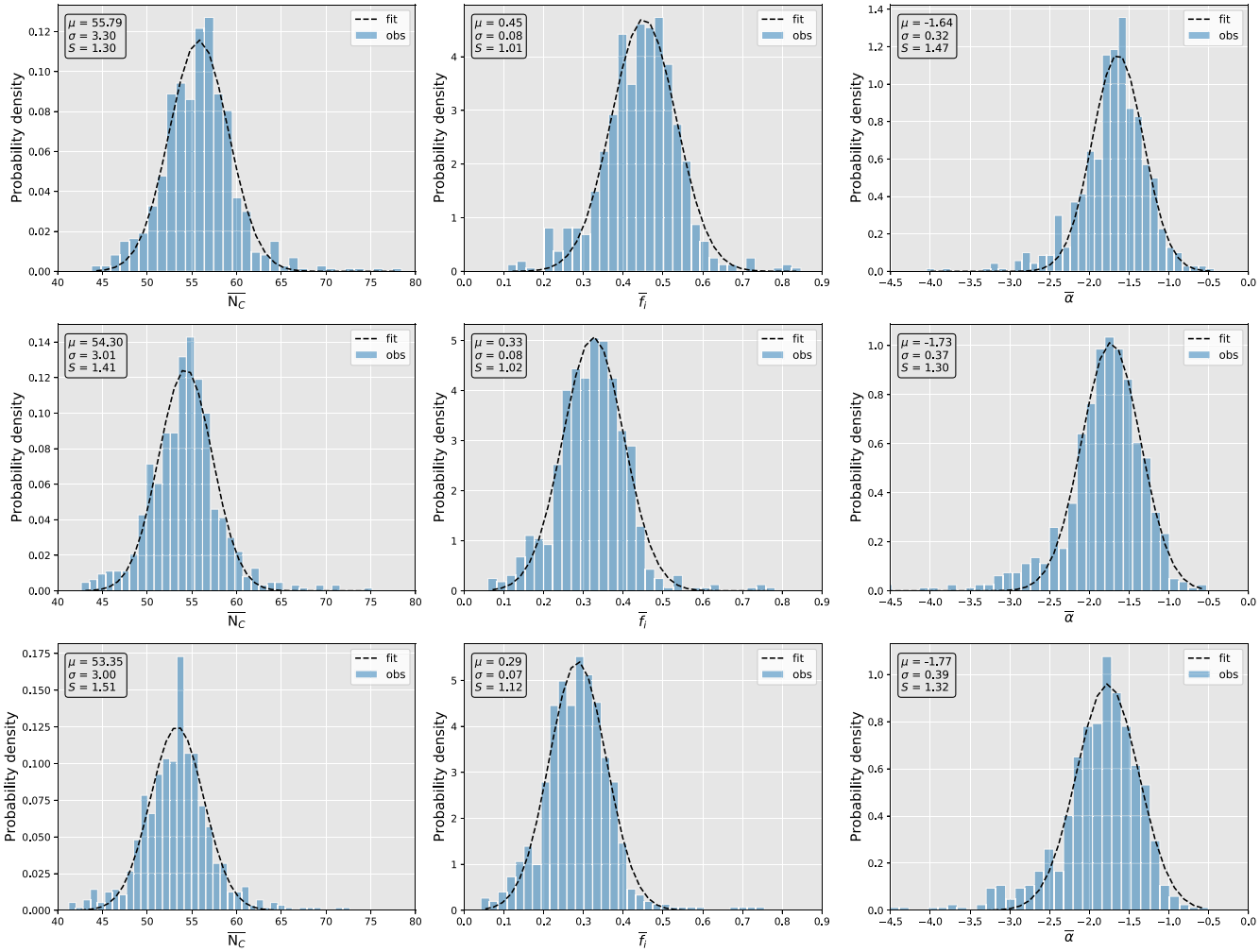

Figure 17. Distributions (Q2) for $\overline{N_C}$ (left panels), $\overline{f_i}$ (middle panels), and $\overline{\alpha}$ (right panels) at excitation energies of 6 eV (top row), 10 eV (middle row), and 12 eV (bottom row). Distributions are fitted with a Gaussian model (black dashed lines). The statistical mean (μ), standard deviation (σ), and skewness (S) are given in the boxes.

Appendix F
The PAHdb-fitted 6.2 μm PAH Band

Here, we compare the 6.2 μm PAH band strength matched by PAHdb and PAHFIT. We use the Q2 spectra with S/N ratios of at least 3 for the 6.2 μm PAH band. To determine the match by PAHdb, we take the average 5.8–7.4 μm fitted spectra from the MC sampling and: *(i)* fit a spline through fixed anchor points to model the blue wing of the broad dust feature component used by PAHFIT at 7.42 μm extending to the 6.2 μm region; *(ii)* use two Gaussians to fit the 6.2 μm PAH band and the smaller blended dust feature component at 6.69 μm as used by PAHFIT. Figure 18 (left panel) demonstrates this approach for the average MC PAHdb-fitted spectrum of the galaxy SDSS J093001.33+390242.0. The right panel of the same figure compares the 6.2 μm PAH band strength determined from the fitted Gaussians and that by PAHFIT. Fitting a straight line returns a slope of 2.13, while the Pearson's coefficient is $r_{xy} = 1.00$.

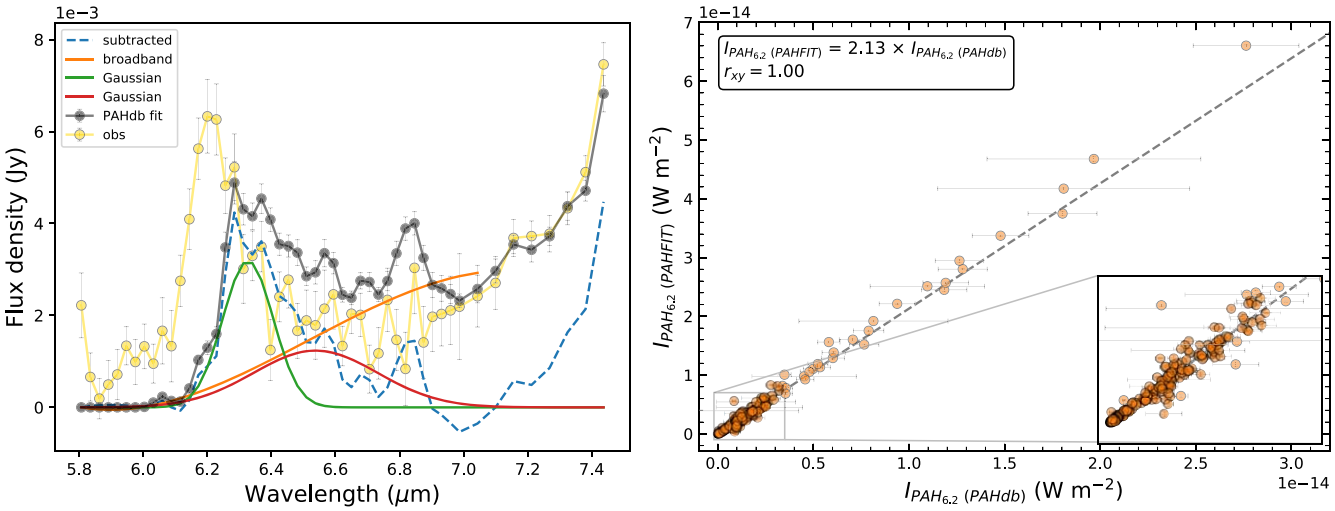

Figure 18. Left: Demonstration of the approach used for determining the amount of the 6.2 μm PAH band matched by PAHdb for the spectrum (black line and points) of the galaxy SDSS J093001.33+390242.0. First, a spline (orange line) is fitted to match the blue wing of the broad dust feature component at 7.42 μm, as employed by PAHFIT, and then is subtracted. The resulting subtracted spectrum (blue dashed line), is fitted with two Gaussians corresponding to the 6.2 and 6.69 μm components used in PAHFIT (green and red lines). The observed PAH spectrum is shown for comparison (yellow line and points). Right: Comparison of the strength of the 6.2 μm PAH band matched by PAHFIT and PAHdb. The gray dashed line shows a straight line fit (slope = 2.13).

Appendix G
Available Online Data

The collected and derived galaxy properties, spectral quality parameters, and PAHFIT-derived PAH band strengths and parameters, as well as the PAHdb-derived parameters, have all been made available online.[15] Table 4 provides an overview of the available data with a short description.

[15] www.astrochemistry.org/pah_galaxy_properties/

Table 4
Available Online Data

Galaxy Properties		PAHFIT-derived Properties		PAHdb-derived Properties	
Column	Description	Column	Description	Column	Description
Galaxy	Galaxy name	Galaxy	Galaxy name	Galaxy	Galaxy name
Sample	Legacy program	Sample	Legacy program	Sample	Legacy program
Class	BPT classification	$I_{6.2}$	6.2 μm PAH band strength	$\overline{N_C}$	Average number of carbon atoms
EQW Class	$EQW_{6.2}$ classification	$I_{6.2\ \mathrm{unc}}$	6.2 μm PAH band strength unc	$\overline{N_C}$ std	Number of carbon atoms std
Dist	Distance	$I_{6.2\ \mathrm{EQW}}$	6.2 μm PAH band EQW	Cation	Cation fraction
z	Redshift	$I_{6.2\ \mathrm{EQW\ unc}}$	6.2 μm PAH band EQW unc	Cation std	Cation fraction std
SFR	Star Formation Rate	$I_{7.7}$	7.7 μm PAH band strength	Small	Small PAHs fraction
M_*	Stellar Mass	$I_{7.7\ \mathrm{unc}}$	7.7 μm PAH band strength unc	Small std	Small PAHs fraction std
sSFR	Specific SFR	$I_{7.7\ \mathrm{EQW}}$	7.7 μm PAH band EQW	Large	Large PAHs fraction
Z	Metallicity	$I_{7.7\ \mathrm{EQW\ unc}}$	7.7 μm PAH band EQW unc	Large std	Large PAHs fraction std
SNR	$S/N_{\ (\mathrm{tot})}$	$I_{8.6}$	8.6 μm PAH band strength	Nitrogen	Nitrogen containing PAH fraction
SNR 11.2	$S/N_{\ (11.2)}$	$I_{8.6\ \mathrm{unc}}$	8.6 μm PAH band strength unc	Nitrogen std	Nitrogen containing PAH fraction std
Q	Quality Class	$I_{8.6\ \mathrm{EQW}}$	8.6 μm PAH band EQW	Pure	Pure PAHs fraction
		$I_{8.6\ \mathrm{EQW\ unc}}$	8.6 μm PAH band EQW unc	Pure std	Pure PAHs fraction std
		$I_{11.2}$	11.2 μm PAH band strength	Ion frac	Ionization fraction
		$I_{11.2\ \mathrm{unc}}$	11.2 μm PAH band strength unc	Ion frac std	Ionization fraction std
		$I_{11.2\ \mathrm{EQW}}$	11.2 μm PAH band EQW	Ioniz param	Ionization parameter
		$I_{11.2\ \mathrm{EQW\ unc}}$	11.2 μm PAH band EQW unc	Ioniz param unc	Ionization parameter unc
		$I_{12.0}$	12.0 μm PAH band strength	a_{eff}	PAH effective radius
		$I_{12.0\ \mathrm{unc}}$	12.0 μm PAH band strength unc	a_{eff} std	PAH effective radius std
		$I_{12.0\ \mathrm{EQW}}$	12.0 μm PAH band EQW	α	a_{eff} distribution power-law index
		$I_{12.0\ \mathrm{EQW\ unc}}$	12.0 μm PAH band EQW unc	α std	a_{eff} distribution power-law index std
		S07 att	$\tau_{9.7}$ silicate	Avg solo	Average number of solo hydrogens
		S07 att unc	$\tau_{9.7}$ silicate unc	Avg solo std	Number of solo hydrogens std
		σ_{pahfit}	PAHFIT unc	Avg duo	Average number of duo hydrogens
		Q	Quality Class	Avg duo std	Number of duo hydrogens std
				Avg trio	Number of trio hydrogens
				Avg trio std	Number of trio hydrogens std
				Avg quartet	Number of quartet hydrogens
				Avg quartet std	Number of quartet hydrogens std
				$I_{3.3}$	3.3 μm PAH band strength
				$I_{3.3\ \mathrm{unc}}$	3.3 μm PAH band strength unc
				σ_{PAHdb}	Average PAHdb unc
				σ_{PAHdb} std	PAHdb unc std
				$\sigma_{PAHdb\ 11.2}$	Average PAHdb 11.2 μm unc
				$\sigma_{PAHdb\ 11.2}$ std	PAHdb 11.2 μm unc std

Appendix H
Comparison between IDL and Python PAHFIT

Figure 19 compares the Q2 6.2, 7.7, and 11.2 μm PAH band strengths determined using the IDL and Python version of PAHFIT. The figure shows good agreement, with most of the scatter for sources with low PAH band strengths. Only galaxies with PAH band strengths greater than 10^{-16} W m^{-2} and S/N ratios of at least 3 are considered.

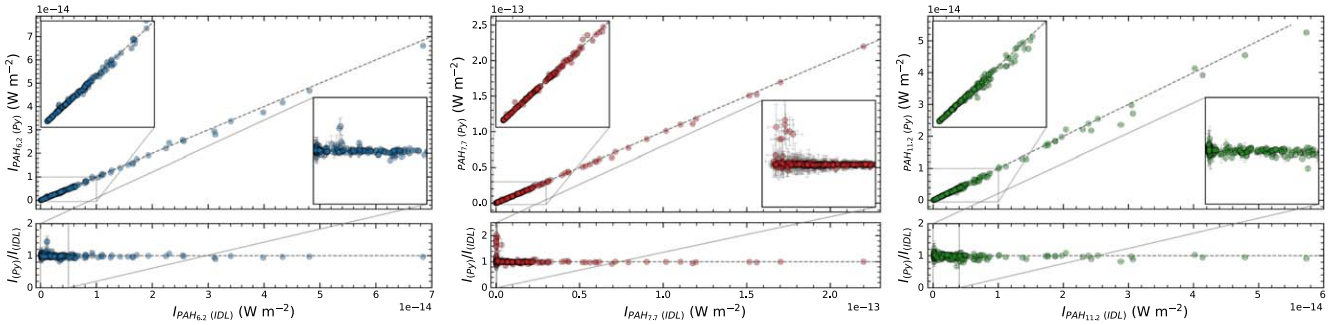

Figure 19. Comparison between the Q2 6.2, 7.7, and 11.2 μm PAH band strengths determined using the IDL and Python version of PAHFIT. Lines of equality are drawn in the upper panels (gray dashed). The bottom panels show the ratio of the Python over IDL PAHFIT-determined PAH band strengths.

ORCID iDs

A. Maragkoudakis https://orcid.org/0000-0003-2552-3871
C. Boersma https://orcid.org/0000-0002-4836-217X
P. Temi https://orcid.org/0000-0002-8341-342X
J. D. Bregman https://orcid.org/0000-0002-1440-5362
L. J. Allamandola https://orcid.org/0000-0002-6049-4079

References

Allamandola, L. J., Hudgins, D. M., & Sandford, S. A. 1999, ApJ, 511, L115
Allamandola, L. J., Tielens, A. G. G. M., & Barker, J. R. 1985, ApJL, 290, L25
Allamandola, L. J., Tielens, A. G. G. M., & Barker, J. R. 1989, ApJS, 71, 733
Alonso-Herrero, A., Ramos Almeida, C., Esquej, P., et al. 2014, MNRAS, 443, 2766
Andrews, H., Boersma, C., Werner, M. W., et al. 2015, ApJ, 807, 99
Armus, L., Charmandaris, V., Bernard-Salas, J., et al. 2007, ApJ, 656, 148
Armus, L., Mazzarella, J. M., Evans, A. S., et al. 2009, PASP, 121, 559
Astropy Collaboration, Price-Whelan, A. M., Sipőcz, B. M., et al. 2018, AJ, 156, 123
Bakes, E. L. O., & Tielens, A. G. G. M. 1994, ApJ, 427, 822
Baldwin, J. A., Phillips, M. M., & Terlevich, R. 1981, PASP, 93, 5
Bauschlicher, C. W. J., Peeters, E., Allamandola, E., et al. 2009, ApJ, 697, 311
Bauschlicher, C. W. J., Ricca, A., Boersma, C., & Allamandola, L. J. 2018, ApJS, 234, 32
Berné, O., Habart, É., Peeters, E., et al. 2022, arXiv:2201.05112
Boersma, C., Bauschlicher, C. W., Allamandola, L. J., et al. 2010, A&A, 511, A32
Boersma, C., Bauschlicher, C. W., Jr., Ricca, A., et al. 2011, ApJ, 729, 64
Boersma, C., Bregman, J., & Allamandola, L. J. 2014a, ApJ, 795, 110
Boersma, C., Bauschlicher, C. W., Jr., Ricca, A., et al. 2014b, ApJS, 211, 8
Boersma, C., Bregman, J., & Allamandola, L. J. 2015, ApJ, 806, 121
Boersma, C., Bregman, J., & Allamandola, L. J. 2016, ApJ, 832, 51
Boersma, C., Bregman, J., & Allamandola, L. J. 2018, ApJ, 858, 67
Boersma, C., Bregman, J. D., & Allamandola, L. J. 2013, ApJ, 769, 117
Boersma, C., Mattioda, A. L., Bauschlicher, C. W., et al. 2009, ApJ, 690, 1208
Bregman, J., & Temi, P. 2005, ApJ, 621, 831
Brinchmann, J., Charlot, S., White, S. D. M., et al. 2004, MNRAS, 351, 1151
Calzetti, D., Kennicutt, R. C., Engelbracht, C. W., et al. 2007, ApJ, 666, 870
Calzetti, D., Wu, S. Y., Hong, S., et al. 2010, ApJ, 714, 1256
Cami, J., Bernard-Salas, J., Peeters, E., & Malek, S. E. 2010, Sci, 329, 1180
Catinella, B., Schiminovich, D., Kauffmann, G., et al. 2010, MNRAS, 403, 683
Chevallard, J., & Charlot, S. 2016, MNRAS, 462, 1415
Chiar, J. E., & Tielens, A. G. G. M. 2006, ApJ, 637, 774
Ciesla, L., Boquien, M., Boselli, A., et al. 2014, A&A, 565, A128
Ciesla, L., Elbaz, D., Schreiber, C., Daddi, E., & Wang, T. 2018, A&A, 615, A61
Cluver, M. E., Jarrett, T. H., Dale, D. A., et al. 2017, ApJ, 850, 68
Conroy, C. 2013, ARA&A, 51, 393
Croiset, B. A., Candian, A., Berné, O., & Tielens, A. G. G. M. 2016, A&A, 590, A26
Dale, D. A., Helou, G., Magdis, G. E., et al. 2014, ApJ, 784, 83
Désesquelles, P., Ha, T. M. H., Korichi, A., et al. 2009, JPhG, 36, 037001
Dopita, M. A., Armus, L., Kewley, L. J., et al. 2011, Ap&SS, 333, 225
Draine, B. T., Aniano, G., Krause, O., et al. 2014, ApJ, 780, 172
Draine, B. T., & Li, A. 2001, ApJ, 551, 807
Draine, B. T., & Li, A. 2007, ApJ, 657, 810
Elbaz, D., Daddi, E., Le Borgne, D., et al. 2007, A&A, 468, 33
Ellison, S. L., Lin, L., Thorp, M. D., et al. 2021, MNRAS, 501, 4777
Enia, A., Rodighiero, G., Morselli, L., et al. 2020, MNRAS, 493, 4107
Esparza-Arredondo, D., González-Martín, O., Dultzin, D., et al. 2018, ApJ, 859, 124
Fleming, B., France, K., Lupu, R. E., & McCandliss, S. R. 2010, ApJ, 725, 159
Galliano, F., Madden, S. C., Tielens, A. G. G. M., Peeters, E., & Jones, A. P. 2008, ApJ, 679, 310
Genzel, R., Lutz, D., Sturm, E., et al. 1998, ApJ, 498, 579
Gordon, K. D., Engelbracht, C. W., Rieke, G. H., et al. 2008, ApJ, 682, 336
Helou, G., Lu, N. Y., Werner, M. W., Malhotra, S., & Silbermann, N. 2000, ApJL, 532, L21
Herrera-Camus, R., Bolatto, A., Smith, J. D., et al. 2016, ApJ, 826, 175
Hony, S., Van Kerckhoven, C., Peeters, E., et al. 2001, A&A, 370, 1030
Hudgins, D. M., Bauschlicher, C. W. J., Allamandola, L. J., et al. 2005, ApJ, 632, 316
Johnson, B. D., Leja, J., Conroy, C., & Speagle, J. S. 2021, ApJS, 254, 22
Kauffmann, G., Heckman, T. M., Tremonti, C., et al. 2003, MNRAS, 346, 1055
Kennicutt, R. C. J., Armus, L., Bendo, G., et al. 2003, PASP, 115, 928
Kewley, L. J., Dopita, M. A., Sutherland, R. S., Heisler, C. A., & Trevena, J. 2001, ApJ, 556, 121
Kewley, L. J., Groves, B., Kauffmann, G., & Heckman, T. 2006, MNRAS, 372, 961
Kewley, L. J., Nicholls, D. C., Sutherland, R., et al. 2019, ApJ, 880, 16
Knuth, K. H. 2006, arXiv:physics/0605197
Kouroumpatzakis, K., Zezas, A., Maragkoudakis, A., et al. 2021, MNRAS, 506, 3079
Lai, T. S. Y., Smith, J. D. T., Baba, S., Spoon, H. W. W., & Imanishi, M. 2020, ApJ, 905, 55
Leger, A., & Puget, J. L. 1984, A&A, 137, L5
Li, A. 2020, NatAs, 4, 339
Li, A., & Draine, B. T. 2001, ApJ, 554, 778
Mackie, C. J., Chen, T., Candian, A., Lee, T. J., & Tielens, A. G. G. M. 2018, JChPh, 149, 134302
Maddox, N., Hess, K. M., Obreschkow, D., Jarvis, M. J., & Blyth, S. L. 2015, MNRAS, 447, 1610
Mahajan, S., Ashby, M. L. N., Willner, S. P., et al. 2019, MNRAS, 482, 560
Maltseva, E., Mackie, C. J., Candian, A., et al. 2018, A&A, 610, A65
Maragkoudakis, A., Ivkovich, N., Peeters, E., et al. 2018a, MNRAS, 481, 5370
Maragkoudakis, A., Zezas, A., Ashby, M. L. N., & Willner, S. P. 2018b, MNRAS, 475, 1485
Maragkoudakis, A., Peeters, E., & Ricca, A. 2020, MNRAS, 494, 642
Maragkoudakis, A., Zezas, A., Ashby, M. L. N., & Willner, S. P. 2017, MNRAS, 466, 1192
Mathis, J. S., Rumpl, W., & Nordsieck, K. H. 1977, ApJ, 217, 425
Mattioda, A. L., Hudgins, D. M., Boersma, C., et al. 2020, ApJS, 251, 22
Mori, T. I., Sakon, I., Onaka, T., et al. 2012, ApJ, 744, 68
Moustakas, J., Kennicutt, R. C., Jr., Tremonti, C. A., et al. 2010, ApJS, 190, 233
Murphy, E. J., Condon, J. J., Schinnerer, E., et al. 2011, ApJ, 737, 67
Nersesian, A., Xilouris, E. M., Bianchi, S., et al. 2019, A&A, 624, A80
O'Dowd, M. J., Schiminovich, D., Johnson, B. D., et al. 2009, ApJ, 705, 885
O'Dowd, M. J., Schiminovich, D., Johnson, B. D., et al. 2011, ApJ, 741, 79

Peeters, E., Bauschlicher, C. W., Jr., Allamandola, L. J., et al. 2017, ApJ, 836, 198
Peeters, E., Hony, S., Van Kerckhoven, C., et al. 2002, A&A, 390, 1089
Puget, J. L., & Leger, A. 1989, ARA&A, 27, 161
Ricca, A., Bauschlicher, C. W. J., Boersma, C., Tielens, A. G. G. M., & Allamandola, L. J. 2012, ApJ, 754, 75
Ricca, A., Boersma, C., & Peeters, E. 2021, ApJ, 923, 202
Riechers, D. A., Pope, A., Daddi, E., et al. 2014, ApJ, 786, 31
Rigopoulou, D., Spoon, H. W. W., Genzel, R., et al. 1999, AJ, 118, 2625
Rosenberg, M. J. F., Berné, O., Boersma, C., Allamandola, L. J., & Tielens, A. G. G. M. 2011, A&A, 532, A128
Sajina, A., Spoon, H., Yan, L., et al. 2009, ApJ, 703, 270
Salim, S., & Narayanan, D. 2020, ARA&A, 58, 529
Sánchez, S. F. 2020, ARA&A, 58, 99
Sandstrom, K. M., Bolatto, A. D., Bot, C., et al. 2012, ApJ, 744, 20
Sandstrom, K. M., Bolatto, A. D., Draine, B. T., Bot, C., & Stanimirović, S. 2010, ApJ, 715, 701
Schawinski, K., Thomas, D., Sarzi, M., et al. 2007, MNRAS, 382, 1415
Schiminovich, D., Charlot, S., da Cunha, E., et al. 2008, S5: The Spitzer SDSS Statistical Spectroscopic Survey, Spitzer Proposal (Pasadena, CA: Caltech), S5
Schutte, W. A., Tielens, A. G. G. M., & Allamandola, L. J. 1993, ApJ, 415, 397
Shannon, M. J., & Boersma, C. 2019, ApJ, 871, 124
Shipley, H. V., Papovich, C., Rieke, G. H., Brown, M. J. I., & Moustakas, J. 2016, ApJ, 818, 60
Silva-Ribeiro, A., Krabbe, A. C., Canelo, C. M., et al. 2022, MNRAS, 509, 327
Smith, J. D. T., Draine, B. T., Dale, D. A., et al. 2007, ApJ, 656, 770
Tielens, A. G. G. M. 2005, The Physics and Chemistry of the Interstellar Medium (Cambridge: Cambridge Univ. Press)
Tielens, A. G. G. M. 2008, ARA&A, 46, 289
Tremonti, C. A., Heckman, T. M., Kauffmann, G., et al. 2004, ApJ, 613, 898
Uchida, K. I., Sellgren, K., Werner, M. W., & Houdashelt, M. L. 2000, ApJ, 530, 817
Weingartner, J. C., & Draine, B. T. 2001, ApJ, 548, 296
Whitaker, K. E., Bezanson, R., van Dokkum, P. G., et al. 2017, ApJ, 838, 19
Whitaker, K. E., van Dokkum, P. G., Brammer, G., & Franx, M. 2012, ApJL, 754, L29
Williams, M. J., Bureau, M., & Cappellari, M. 2010, MNRAS, 409, 1330
Wu, Y., Helou, G., Armus, L., et al. 2010, ApJ, 723, 895
Xie, Y., & Ho, H. C. 2022, ApJ, 925, 218
Xie, Y., Ho, L. C., Li, A., & Shangguan, J. 2018, ApJ, 860, 154
Zang, R. X., Peeters, E., & Boersma, C. 2019, ApJ, 887, 46